

Supporting Information

for

Global aviation contrail climate effects from 2019 to 2021

Roger Teoh¹, Zebediah Engberg², Ulrich Schumann³, Christiane Voigt^{3,4}, Marc Shapiro²,
Susanne Rohs⁵ and Marc E.J. Stettler^{1*}

¹ Centre for Transport Studies, Department of Civil and Environmental Engineering, Imperial College London,
London, SW7 2AZ, United Kingdom

² Breakthrough Energy, 4110 Carillon Point, Kirkland, WA 98033, United States

³ Institute of Atmospheric Physics, Deutsches Zentrum für Luft- und Raumfahrt, 82234 Oberpfaffenhofen,
Germany

⁴ Institute of Atmospheric Physics, University Mainz, 55099 Mainz, Germany

⁵ IEK-8 Troposphäre, Institut für Energie und Klimaforschung, Forschungszentrum Jülich GmbH, Jülich,
Germany

* Corresponding author: m.stettler@imperial.ac.uk

Supporting Information Details:

- Number of pages: 41
- Number of figures: 20
- Number of tables: 13

24 **Table of Contents**

25 S1 Meteorology.....3

26 S1.1 ERA5 high-resolution realization.....3

27 S1.2 Existing corrections to ERA5 humidity fields.....5

28 S1.3 Global humidity correction.....6

29 S2 CoCiP model outputs.....13

30 S3 Global contrail simulation.....15

31 S4 Sensitivity analysis.....26

32 S4.1 Extended humidity correction.....29

33 S4.2 Radiative heating effects.....30

34 S4.3 Contrail-contrail overlapping.....31

35 S5 Comparison with other studies.....35

36 References.....37

37

38

39 S1 Meteorology

40 S1.1 ERA5 high-resolution realization

41 In this study, we use meteorological and radiation data from the European Centre for Medium-
42 Range Weather Forecast (ECMWF) Reanalysis 5th Generation (ERA5) high-resolution
43 realization (HRES) to perform the global contrail simulation (Hersbach et al., 2020). The ERA5
44 HRES is publicly available from the ECMWF Copernicus Climate Data Store (ECMWF, 2021)
45 and the following variables are downloaded at a spatiotemporal resolution of $0.25^\circ \times 0.25^\circ$
46 over 37 pressure levels for meteorological variables (or 1 level for radiation variables) and at a
47 1 h temporal resolution:

- 48 • specific humidity (in kg kg^{-1}),
- 49 • air temperature (in K),
- 50 • eastward and northward wind (in m s^{-1}),
- 51 • lagrangian tendency of air pressure, i.e., vertical velocity (in Pa s^{-1}),
- 52 • specific cloud ice water content (in kg kg^{-1}),
- 53 • fraction of cloud cover,
- 54 • geopotential (in $\text{m}^2 \text{s}^{-2}$),
- 55 • top of atmosphere incident solar radiation (in J m^{-2}),
- 56 • top of atmosphere net upward shortwave flux (in J m^{-2}), and
- 57 • top of atmosphere outgoing longwave flux (in J m^{-2}).

58 Meteorology at each waypoint is obtained using a quadrilinear interpolation across space
59 (longitude, latitude, and pressure level) and time. We calculate the relative humidity with
60 respect to liquid water (RH) and relative humidity with respect to ice (RH_i) using the following
61 equations from Sonntag (1994),

$$RH = \frac{p_w q_w R_1}{p_{liq} R_0}, \quad (S1)$$

$$RH_i = \frac{p_w q_w R_1}{p_{ice} R_0}. \quad (S2)$$

62 where p_w is the pressure altitude for each waypoint (in Pa), q_w is the specific humidity, R_0
 63 ($287.05 \text{ J kg}^{-1} \text{ K}^{-1}$) and R_1 ($461.51 \text{ J kg}^{-1} \text{ K}^{-1}$) are the real gas constant for air and water vapour
 64 respectively, and the saturation pressure of water vapour over liquid water (p_{liq} , in Pa) and ice
 65 (p_{ice} , in Pa) are calculated based on air temperature (T_w) (Sonntag, 1994),

$$p_{liq} = 100 \exp \left[\frac{-6096.9385}{T_w} + 16.635794 - 0.02711193 T_w + (1.673952 \times 10^{-5}) T_w^2 + 2.433502 \ln(T_w) \right], \quad (S3)$$

$$p_{ice} = 100 \exp \left[\frac{-6024.5282}{T_w} + 24.721994 + 0.010613868 T_w - (1.3198825 \times 10^{-5}) T_w^2 - 0.49382577 \ln(T_w) \right]. \quad (S4)$$

66 The simulated contrail properties and lifetime have been shown to be highly sensitive to the
 67 RH_i (Schumann et al., 2021; Teoh et al., 2022). However, existing studies have identified
 68 several limitations in the humidity fields provided by ECMWF ERA5 products. An assessment
 69 of the ERA5 humidity fields showed that the ERA5-derived ice supersaturated regions (ISSR)
 70 coverage area could be overestimated by up to 100% when compared with radiosonde
 71 measurements (Agarwal et al., 2022), or underestimated relative to in-situ humidity
 72 measurements from the In-Service Aircraft for a Global Observing System (IAGOS) campaign
 73 (Reutter et al., 2020). In addition, the magnitude of RH_i within the ERA5-derived ISSR are
 74 generally weakly supersaturated (RH_i \approx 100%) and do not generally exceed RH_i > 120%
 75 (Reutter et al., 2020; Gierens et al., 2020; Teoh et al., 2022). The low variability in RH_i
 76 magnitude is most likely caused by simplified assumptions adopted in the ERA5 products
 77 where the relaxation time, i.e., time required for the excess supersaturated humidity to be
 78 deposited into ambient particles and ice crystals and reach equilibrium (RH_i \approx 100%), is
 79 currently set to one model time step (Tompkins et al., 2007; Koop et al., 2000). In addition, the
 80 spatiotemporal resolution of existing meteorological datasets is not sufficient to capture the
 81 sub-grid scale variability and localised air pockets with RH_i > 120%. Therefore, the use of

82 ERA5 products for contrail simulation can lead to errors and uncertainties in the simulated
83 contrail lifetime, properties, and climate forcing (Teoh et al., 2022; Agarwal et al., 2022;
84 Gierens et al., 2020).

85 **S1.2 Existing corrections to ERA5 humidity fields**

86 Studies that simulated contrails with the contrail cirrus prediction model (CoCiP) have
87 formulated different approaches to account for the known limitations in the humidity fields
88 provided by ECMWF products. In particular, earlier studies used an enhancement factor (RH_{ic})
89 to uniformly increase the RH_i (Schumann, 2012; Schumann et al., 2015; Teoh et al., 2020;
90 Schumann et al., 2021),

$$RH_{i\text{Corrected}} = \frac{RH_i}{RH_{ic}}, \quad (S5)$$

91 where the RH_{ic} was set to 0.90 or 0.95 depending on the ECMWF product used
92 (reanalysis/forecast), its spatiotemporal resolution, and/or the spatial domain of the simulation.
93 While the rationale of Eq. (S5) was to increase the mean RH_i so that the corrected humidity
94 fields are no longer weakly supersaturated, there are inherent limitations where: (i) the
95 correction leads to a larger ISSR coverage area and could cause the simulated contrail
96 formation, lifetime and climate forcing to be overestimated (Agarwal et al., 2022); and (ii) it
97 does not produce an RH_i distribution that is consistent with in-situ measurements from the
98 IAGOS campaign (Teoh et al., 2022).

99 To address these issues, Teoh et al. (2022) used in-situ humidity measurements from the
100 IAGOS campaign (Petzold et al., 2020; Boulanger et al., 2022) to develop a new humidity
101 correction methodology for the North Atlantic region,

$$\text{RHi}_{\text{corrected}} = \begin{cases} \frac{\text{RHi}}{a_{\text{opt}}} & , \text{ when } \left(\frac{\text{RHi}}{a_{\text{opt}}} \right) \leq 1 \\ \min \left(\left(\frac{\text{RHi}}{a_{\text{opt}}} \right)^{b_{\text{opt}}}, \text{RHi}_{\text{max}} \right) & , \text{ when } \left(\frac{\text{RHi}}{a_{\text{opt}}} \right) > 1 \end{cases} \quad (\text{S6})$$

102 where $\text{RHi}_{\text{max}} = 1.65$, $a_{\text{opt}} = 0.9779$ and $b_{\text{opt}} = 1.635$ are calibrated coefficients to minimise the
103 Cramer-von Mises (CvM) test statistic, a measure of the goodness of fit between two
104 probability density functions (Parr and Schucany, 1980). This correction methodology
105 addresses the two limitations from the earlier approach, i.e. Eq. (S5), where: (i) the false
106 positive ($N_{\text{IAGOS}}/Y_{\text{HRES}}$, where the ERA5 HRES derived RHi indicates that the waypoint is in
107 ISSR but not in the IAGOS measurements) and false negative ($Y_{\text{IAGOS}}/N_{\text{HRES}}$) rates are
108 generally symmetrical which should lead to the cancelling out of errors in ISSR and contrail
109 occurrence over the spatiotemporal domain; and (ii) the distribution of $\text{RHi}_{\text{corrected}}$ is now
110 consistent with in-situ RHi measurements from IAGOS (refer to Fig. S9 in Teoh et al. (2022)).
111 Using Eq. (S6), the 2019 annual mean contrail cirrus net radiative forcing (RF) over the North
112 Atlantic increased from 121 mW m^{-2} (no humidity correction) to 235 mW m^{-2} , indicating that
113 the simulated contrail climate forcing is highly sensitive to the provided humidity fields (Teoh
114 et al., 2022). However, we also note that the correction was formulated using RHi
115 measurements in the North Atlantic and therefore, the calibrated coefficients (a_{opt} and b_{opt})
116 might not be valid when applied across the globe.

117 **S1.3 Global humidity correction**

118 Here, we use the full (global) IAGOS dataset (Petzold et al., 2020; Boulanger et al., 2022) to
119 extend the humidity correction methodology from Teoh et al. (2022) so it can be applied to the
120 global contrail simulation. The IAGOS dataset provides the aircraft position (longitude,
121 latitude, pressure level and time) and measurements of q_w and T_w at a $\sim 4 \text{ s}$ time interval from
122 2,161 distinct flights in 2019. For each flight, we excluded waypoints that are below 25,000
123 feet and resampled the time series data to obtain the mean q_w and T_w at a frequency of 60 s to

124 minimise the autocorrelation between data points (Gierens et al., 2020), and the resampled
 125 dataset consists of 682,308 unique waypoints. Fig. S1 and S2 shows the spatial distribution of
 126 the waypoints where q_w and T_w were measured: ~95% of the data points were measured in the
 127 Northern Hemisphere, of which ~63% of them were between 20–50°N, and ~69% of the
 128 measurements were at altitudes between 35,000 and 40,000 feet.

129 The RHi for each waypoint is calculated using: (i) Eq. (S2) and (S4) with in-situ measurements
 130 of q_w and T_w , hereby known as RHi_{IAGOS} ; and (ii) a quadrilinear interpolation from the ERA5
 131 HRES humidity fields. To avoid statistical bias and oversampling at specific latitude bands, we
 132 split the IAGOS dataset into latitude bins of 10° intervals. Table S1 compares RHi_{IAGOS} with
 133 the RHi derived from the original ERA5 HRES humidity fields for each latitude bin. An
 134 analysis of the false positive (N_{IAGOS}/Y_{HRES}) and false negative (Y_{IAGOS}/N_{HRES}) rates shows that
 135 the RHi errors have a latitude dependence, where the ERA5-derived ISSR coverage area could
 136 be: (i) overpredicted at the tropics and subtropics (0–40°N); and (ii) underpredicted at higher
 137 latitudes above 40°N.

138 **Table S1: Comparison of the ISSR occurrence from the IAGOS measurements versus those derived from**
 139 **the uncorrected humidity fields from the ERA5 HRES. Y_{IAGOS} indicates that the waypoint has an RHi >**
 140 **100% (ISSR occurrence) according to the IAGOS measurements, while N_{IAGOS} indicates the opposite. The**
 141 **subscript “HRES” is used to indicate ISSR occurrence as provided by the ERA5 HRES.**

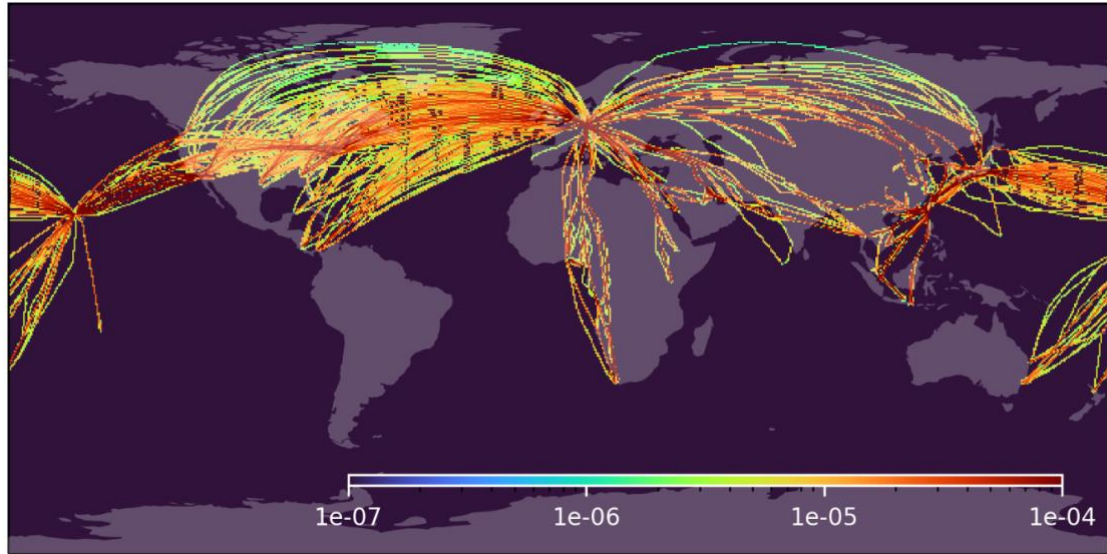
| No RHi correction | No. of waypoints | Y_{IAGOS}/Y_{HRES} (%) | N_{IAGOS}/N_{HRES} (%) | Y_{IAGOS}/N_{HRES} (%) | N_{IAGOS}/Y_{HRES} (%) | Ratio ^a | CvM stat ^b | ETS ^c |
|-------------------|------------------|--------------------------|--------------------------|--------------------------|--------------------------|--------------------|-----------------------|------------------|
| 0 - 10°N | 20650 | 9.16 | 70.1 | 8.22 | 12.5 | -0.341 | 58.2 | 0.207 |
| 10 - 20°N | 48366 | 5.02 | 83.2 | 5.67 | 6.06 | -0.064 | 73.0 | 0.246 |
| 20 - 30°N | 144910 | 2.90 | 90.1 | 2.90 | 4.08 | -0.290 | 43.7 | 0.264 |
| 30 - 40°N | 141131 | 4.42 | 87.7 | 3.69 | 4.14 | -0.110 | 93.1 | 0.322 |
| 40 - 50°N | 114018 | 5.40 | 85.1 | 6.24 | 3.31 | 0.889 | 261 | 0.315 |
| 50 - 60°N | 106993 | 6.75 | 83.1 | 6.39 | 3.73 | 0.714 | 232 | 0.347 |
| 60 - 90°N | 33762 | 5.57 | 87.0 | 5.06 | 2.33 | 1.169 | 91.7 | 0.390 |

142 ^a: Ratio compares the false positive and false negative rate and is computed by $(\frac{N_{IAGOS}/Y_{HRES}(\%)}{Y_{IAGOS}/N_{HRES}(\%)} - 1)$. A positive value indicates
 143 that the ERA5 HRES underpredicts contrails, a value of zero indicates a symmetrical false positive and false negative rate,
 144 while a negative value indicates that the ERA5 HRES overpredicts contrails.

145 ^b: CvM test statistic, where a lower value indicates a better goodness-of-fit between the probability density function of the
 146 measured and ERA5-derived RHi.

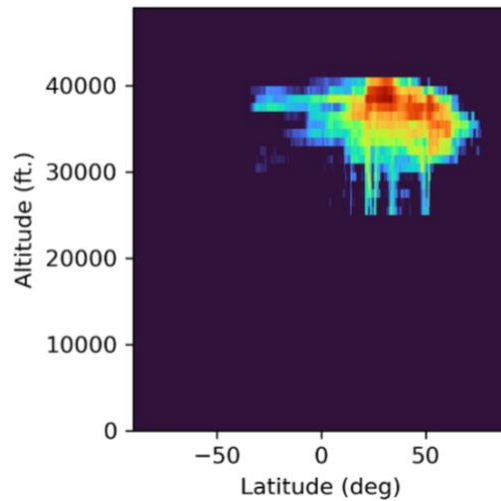
147 ^c: The equitable threat score (ETS) is calculated according to Appendix A of Gierens et al. (Gierens et al., 2020), where ETS =
 148 1 indicates that the ERA5-derived RHi is in perfect agreement with measurements, ETS = 0 indicates a completely random
 149 relationship, while ETS < 0 indicates an inverse relationship between the measured and ERA5-derived RHi.

150



151

152 **Figure S1: Spatial distribution of the data points provided by the resampled IAGOS dataset, where the**
 153 **colour bar represents the normalised density at each pixel (682,308 waypoints from 2,161 unique flights).**
 154 **Basemap plotted using Cartopy 0.21.1 © Natural Earth; license: public domain.**



155

156 **Figure S2: Distribution of the data points provided by the resampled IAGOS dataset by latitude and**
 157 **altitude (682,308 waypoints from 2,161 unique flights).**

158 **Table S2: a_{opt} and b_{opt} coefficients for each latitude band that is calibrated using the full IAGOS dataset**
 159 **and a bootstrap resampling method (n=1000) that provides an estimate of their respective standard errors.**

| | a_{opt} | | b_{opt} | |
|------------------|--------------|-------------------------|--------------------|------------------------|
| | Full dataset | Bootstrap ^a | Full dataset | Bootstrap ^a |
| 0 - 10°N | 1.022 | 1.038 [1.019, 1.056] | 2.900 ^b | 2.900 ^b |
| 10 - 20°N | 1.003 | 1.023 [1.013, 1.034] | 2.672 | 2.664 [2.539, 2.813] |
| 20 - 30°N | 1.020 | 1.019 [1.013, 1.025] | 1.516 | 1.519 [1.453, 1.586] |
| 30 - 40°N | 1.007 | 1.011 [1.006, 1.019] | 1.445 | 1.448 [1.398, 1.492] |
| 40 - 50°N | 0.9563 | 0.9644 [0.9547, 0.9750] | 1.633 | 1.632 [1.594, 1.680] |
| 50 - 60°N | 0.9641 | 0.9782 [0.9688, 0.9875] | 1.320 | 1.325 [1.289, 1.359] |
| 60 - 90°N | 0.9406 | 0.9099 [0.8734, 0.9430] | 1.336 | 1.340 [1.266, 1.498] |

160 ^a: The bootstrap resampling method is used to estimate the mean a_{opt} and b_{opt} for each latitude band and their respective standard
 161 error [1st percentile, 99th percentile].

162 ^b: The b_{opt} for this latitude band is constrained to 2.9 to prevent the corrected RHi in having unrealistic values.

163 Based on these results, we use Eq. (S6) as a basis to extend the humidity correction
 164 methodology from Teoh et al. (2022) and capture these latitude effects. The a_{opt} and b_{opt}
 165 coefficients are optimised for each latitude bin: the first step involves optimising a_{opt} with the
 166 objective function of yielding a symmetrical false positive and false negative rate so that errors
 167 in the ISSR occurrence cancel each other out; and b_{opt} is then optimised by minimising the
 168 CvM test statistic (Parr and Schucany, 1980) so that the ERA5-derived RHi has a probability
 169 density function that is consistent with $\text{RHi}_{\text{IAGOS}}$. Table S2 summarises the a_{opt} and b_{opt}
 170 coefficients for each latitude band that is calibrated using: (i) the full dataset; and (ii) a bootstrap
 171 resampling method that estimates their respective standard errors and used to approximate their
 172 uncertainty range. We then fit the derived a_{opt} and b_{opt} from (i) with a sigmoid function to
 173 account for the rapid change tropopause height between 20° and 50° N/S (Santer et al., 2003),

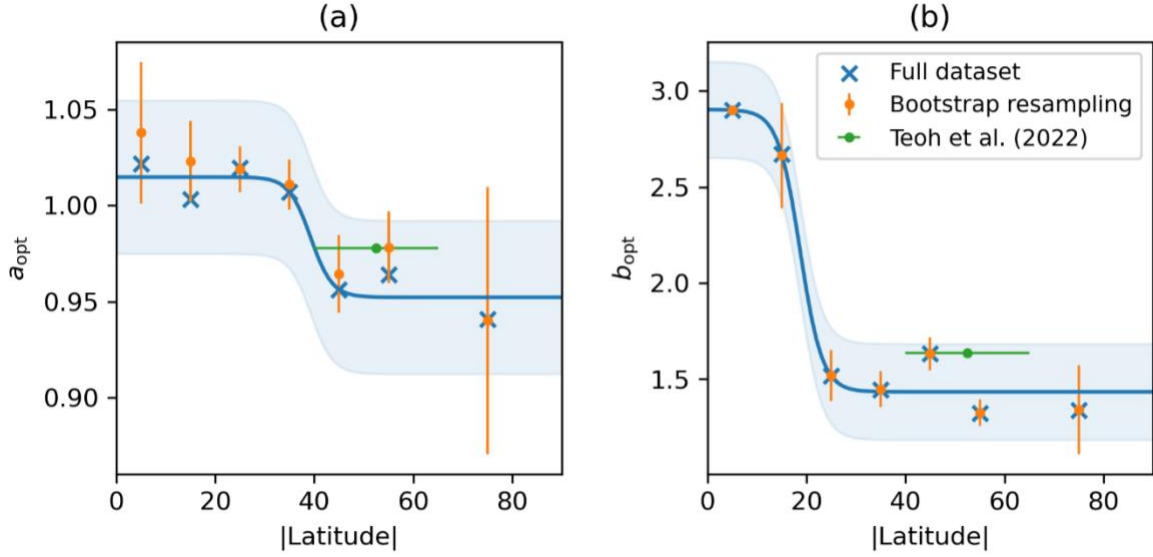
$$a_{\text{opt}} = \frac{a_0}{1 + \exp(a_1 \times (|\text{lat}| - a_2))} + a_3, \quad (\text{S7})$$

$$b_{\text{opt}} = \frac{b_0}{1 + \exp(b_1 \times (|\text{lat}| - b_2))} + b_3, \quad (\text{S8})$$

174 where $a_0 = 0.06262$, $a_1 = 0.4589$, $a_2 = 39.25$ and $a_3 = 0.9522 \pm 0.04$, and $b_0 = 1.471$, $b_1 = 0.4431$,
 175 $b_2 = 18.76$ and $b_3 = 1.433 \pm 0.25$. The range of a_3 and b_3 is specified to cover the uncertainty
 176 range of a_{opt} and b_{opt} that is derived from the bootstrap resampling method (Fig. S3). Given the
 177 limited number of waypoints below 0°N (< 5% of all data points in the IAGOS dataset), we
 178 use the absolute latitude values in Eq. (S7) and (S8) assuming that the latitude effects are
 179 symmetrical between the Northern and Southern Hemisphere. The RHi_{max} term in Eq. (S6) is
 180 also revised and calculated as a function of T_w to ensure that the $\text{RHi}_{\text{corrected}}$ is within the
 181 maximum value permissible by thermodynamics (i.e., $\text{RH} < 100\%$, and below the threshold
 182 that leads to homogeneous ice nucleation and formation of natural cirrus clouds) (Pruppacher
 183 et al., 2007; Kärcher and Lohmann, 2002; Tompkins et al., 2007),

$$\text{RHi}_{\max} = \begin{cases} \frac{p_{\text{liq}}(T_w)}{p_{\text{ice}}(T_w)} & , \text{ when } T_w > 235 \text{ K} \\ 1.67 + (1.45 - 1.67) \times \frac{(T_w - 190)}{(235 - 190)} & , \text{ when } T_w \leq 235 \text{ K} \end{cases} \quad (\text{S9})$$

184 where $p_{\text{liq}}(T_w)$ and $p_{\text{ice}}(T_w)$ are estimated using Eq. (S3) and (S4) respectively.



185

186 **Figure S3: Visualisation of Eq. (S7) and (S8), where a sigmoid is used to fit (a) a_{opt} and (b) b_{opt} as a function**
 187 **of latitude. The vertical lines from the bootstrap resampling method (orange data points) represent the 1st**
 188 **and 99th percentile of the standard error, and the shaded regions approximate the uncertainty of a_{opt} and**
 189 **b_{opt} . The a_{opt} and b_{opt} derived from an earlier study in the North Atlantic region (Teoh et al., 2022) is also**
 190 **plotted as green data points.**

191 **Table S3: Comparison of the ISSR occurrence derived from $\text{RHi}_{\text{IAGOS}}$ versus those derived from the**
 192 **corrected humidity fields from the ERA5 HRES using Eq. (S6) to Eq. (S9). Y_{IAGOS} indicates that the**
 193 **waypoint has an $\text{RHi} > 100\%$ (ISSR occurrence) according to the IAGOS measurements, while N_{IAGOS}**
 194 **indicates the opposite. The subscript ‘‘HRES’’ is used to indicate ISSR occurrence as provided by the ERA5**
 195 **HRES.**

| Global humidity correction | $Y_{\text{IAGOS}}/Y_{\text{HRES}}$ (%) | $N_{\text{IAGOS}}/N_{\text{HRES}}$ (%) | $Y_{\text{IAGOS}}/N_{\text{HRES}}$ (%) | $N_{\text{IAGOS}}/Y_{\text{HRES}}$ (%) | Ratio ^a | CvM stat ^b | ETS ^c |
|----------------------------|--|--|--|--|--------------------|-----------------------|------------------|
| 0 - 10°N | 7.82 | 71.8 | 9.56 | 10.9 | -0.119 | 2.09 | 0.183 |
| 10 - 20°N | 4.44 | 84.1 | 6.25 | 5.21 | 0.199 | 2.55 | 0.229 |
| 20 - 30°N | 2.58 | 90.7 | 3.22 | 3.50 | -0.080 | 9.93 | 0.249 |
| 30 - 40°N | 4.28 | 88.0 | 3.83 | 3.87 | -0.010 | 24.2 | 0.319 |
| 40 - 50°N | 6.70 | 83.7 | 4.94 | 4.69 | 0.054 | 1.06 | 0.358 |
| 50 - 60°N | 8.40 | 81.5 | 4.74 | 5.40 | -0.122 | 22.3 | 0.394 |
| 60 - 90°N | 6.93 | 86.1 | 3.70 | 3.28 | 0.128 | 0.360 | 0.456 |

196 ^a: Ratio compares the false positive and false negative rate and is computed by $(\frac{N_{\text{IAGOS}}/Y_{\text{HRES}} (\%)}{Y_{\text{IAGOS}}/N_{\text{HRES}} (\%)} - 1)$. A positive value indicates
 197 that the ERA5 HRES underpredicts contrails, a value of zero indicates a symmetrical false positive and false negative rate,
 198 while a negative value indicates that the ERA5 HRES overpredicts contrails.

199 ^b: CvM test statistic, where a lower value indicates a better goodness-of-fit between the probability density function of the
 200 measured and ERA5-derived RHi.

201 ^c: The equitable threat score (ETS) is calculated according to Appendix A of Gierens et al. (Gierens et al., 2020), where ETS =
 202 1 indicates that the ERA5-derived RHi is in perfect agreement with measurements, ETS = 0 indicates a completely random
 203 relationship, while ETS < 0 indicates an inverse relationship between the measured and ERA5-derived RHi.

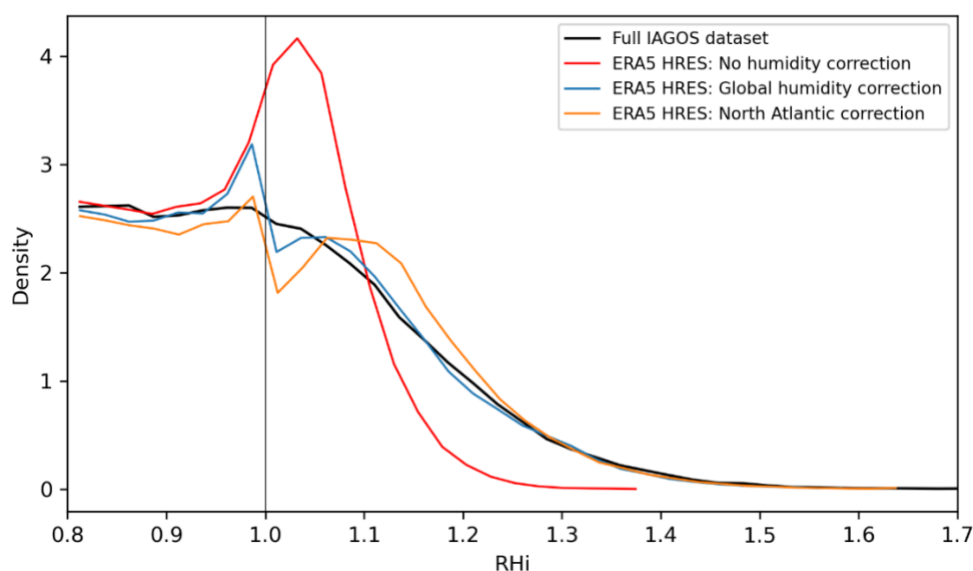
204 **Table S4: Performance metrics comparing the agreement between the RH_i measurements provided by**
 205 **the full IAGOS dataset versus the uncorrected and corrected ERA5 HRES global humidity fields.**

| Full IAGOS dataset vs. ERA5 HRES | Correct prediction (%) | Ratio ^a | Mean CvM statistic ^b | Mean ETS ^c |
|--|------------------------|--------------------|---------------------------------|-----------------------|
| Uncorrected humidity fields | 89.4 | 0.281 | 122 | 0.299 |
| Global humidity correction | 89.6 | 0.007 | 8.93 | 0.313 |
| North Atlantic correction (Teoh et al.(Teoh et al., 2022)) | 89.1 | -0.076 | 35.40 | 0.319 |

206 ^a: Ratio compares the false positive and false negative rate and is computed by $(\frac{N_{IAGOS}/Y_{HRES}(\%)}{Y_{IAGOS}/N_{HRES}(\%)} - 1)$. A positive value indicates
 207 that the ERA5 HRES underpredicts contrails, a value of zero indicates a symmetrical false positive and false negative rate,
 208 while a negative value indicates that the ERA5 HRES overpredicts contrails.

209 ^b: CvM test statistic, where a lower value indicates a better goodness-of-fit between the probability density function of the
 210 measured and ERA5-derived RH_i.

211 ^c: The equitable threat score (ETS) is calculated according to Appendix A of Gierens et al.(Gierens et al., 2020), where ETS =
 212 1 indicates that the ERA5-derived RH_i is in perfect agreement with measurements, ETS = 0 indicates a completely random
 213 relationship, while ETS < 0 indicates an inverse relationship between the measured and ERA5-derived RH_i.



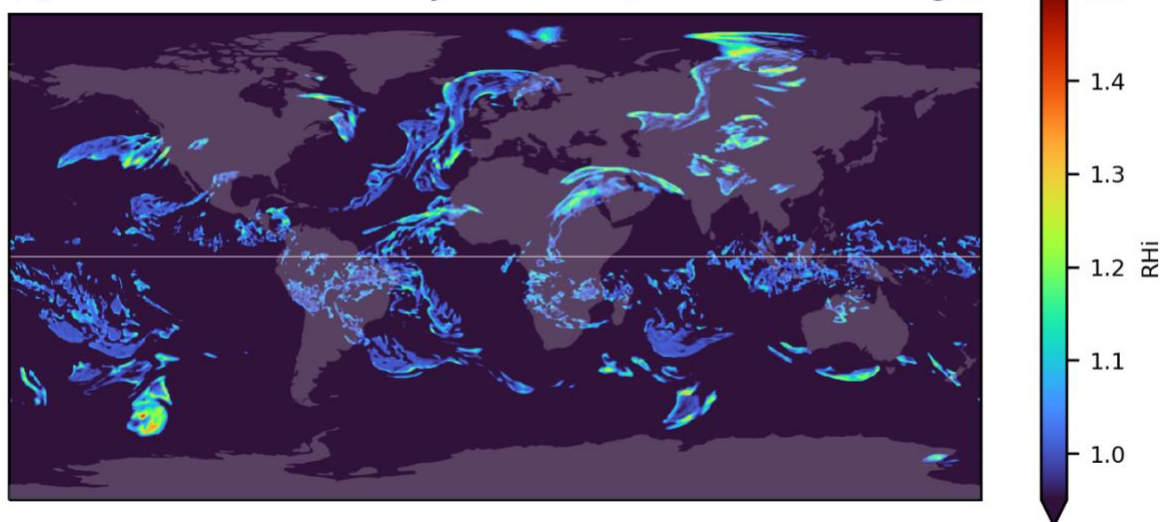
214 **Figure S4: Probability density function of the RH_i measurements provided by the full IAGOS dataset**
 215 **(black line) versus those derived from the ERA5 HRES with: (i) no humidity correction (red line); (ii) the**
 216 **global humidity correction (blue line); and (iii) the North Atlantic correction previously developed by Teoh**
 217 **et al. (2022) (orange line).**

219 When evaluated using four different performance metrics, the global humidity correction
 220 generally improved the agreement between RH_{iIAGOS} and RH_{iCorrected} for each latitude bin
 221 (Table S3 vs. Table S1). Table S4 summarises the performance metrics when the full IAGOS
 222 dataset is compared with the uncorrected and corrected ERA5 HRES global humidity fields,
 223 showing significant improvements where the:

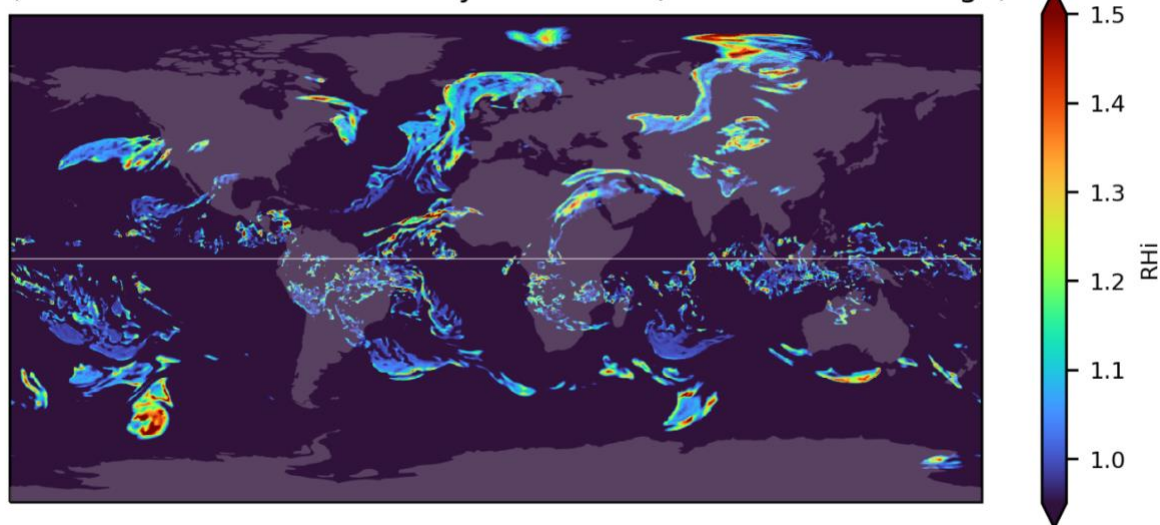
- 224 • percentage of waypoints with the correct prediction of ISSR occurrence (Y_{IAGOS}/Y_{HRES}
 225 and N_{IAGOS}/N_{HRES}) increased slightly from 89.4% to 89.6%,

- 226 • false positive (N_{IAGOS}/Y_{HRES}) and false negative (Y_{IAGOS}/N_{HRES}) rates are now
227 symmetrical, meaning that errors in the ISSR occurrence and persistent contrail
228 formation are expected to cancel out over the spatiotemporal domain,
- 229 • CvM test statistic reduced by 93% (from 122 to 8.93), which implies a significant
230 improvement in the goodness-of-fit between the probability density function of
231 RH_{IAGOS} and $RH_{corrected}$ (Fig. S4), and
- 232 • the mean ETS improved by 4.7% from 0.299 to 0.313.

(a) ERA5 HRES: No humidity correction (9.93% ISSR coverage)

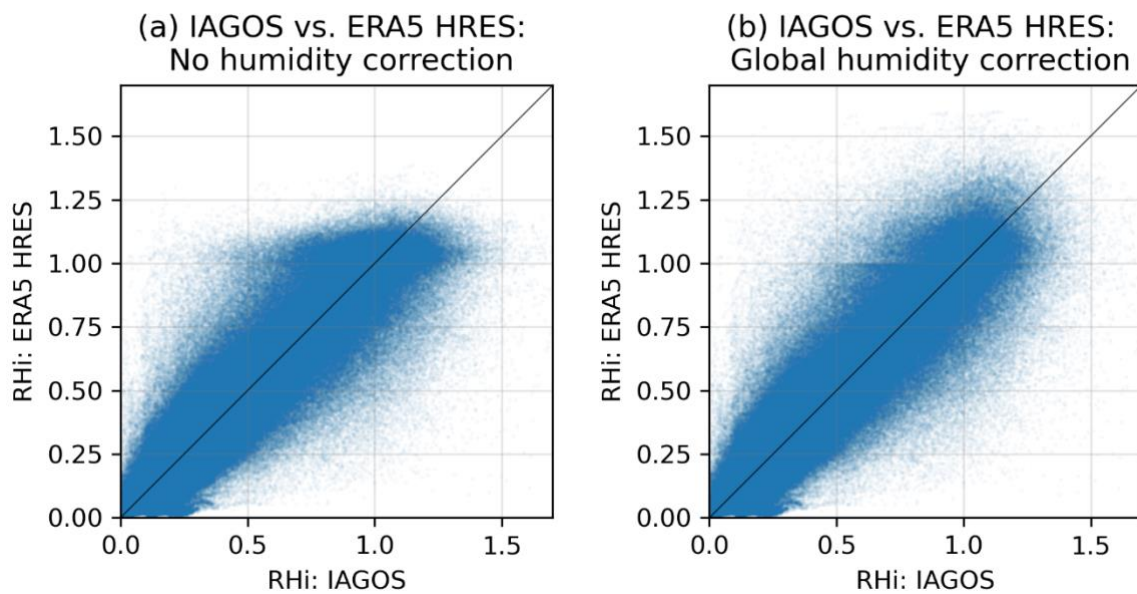


(b) ERA5 HRES: Global humidity correction (9.11% ISSR coverage)



233
234 **Figure S5: Comparison of the magnitude and spatial distribution of the: (a) original RHi fields provided**
235 **by the ERA5 HRES; versus (b) the corrected RHi fields from the global humidity correction at pressure**
236 **level 22500 Pa (36,000 feet) on 1-January-2020 00:00:00 (UTC). Basemap plotted using Cartopy 0.21.1 ©**
237 **Natural Earth; license: public domain.**

238 Fig. S5 visualises the change in magnitude and spatial distribution of the ERA5-derived RH_i.
 239 It shows that the global humidity correction leads to: (i) a small reduction in ISSR coverage
 240 area at the tropics; (ii) an increase in ISSR coverage area at latitudes above 40°N and below
 241 40°S; and (iii) a higher occurrence of localised regions with very high ice supersaturation (RH_i
 242 > 140%). While the global humidity correction ensures that the RH_i distribution derived from
 243 the ERA5 HRES is more consistent with RH_iIAGOS (Fig. S4), we note that: (i) there is a residual
 244 peak in RH_icorrected at close to 1.0 (Fig. S4) because humidity in a waypoint is only scaled
 245 upwards when $a_{opt} < 1$ and $RH_{i\text{waypoint}} > \left(\frac{RH_i}{a_{opt}}\right)$; and (ii) RH_i uncertainties at the individual
 246 waypoint level remains large (Fig. S6). Both issues should be addressed in future research.



247
 248 **Figure S6: Parity plots comparing the RH_i derived from in-situ measurements from the IAGOS campaign**
 249 **relative to: (a) the original RH_i derived from the ERA5 HRES; and (b) the RH_i when the global humidity**
 250 **correction is applied to the ERA5 HRES (n = 682,308).**

251 S2 CoCiP model outputs

252 CoCiP is used to simulate the evolution and lifecycle of each contrail segment (Schumann,
 253 2012; Schumann et al., 2012), and five different output formats are available:

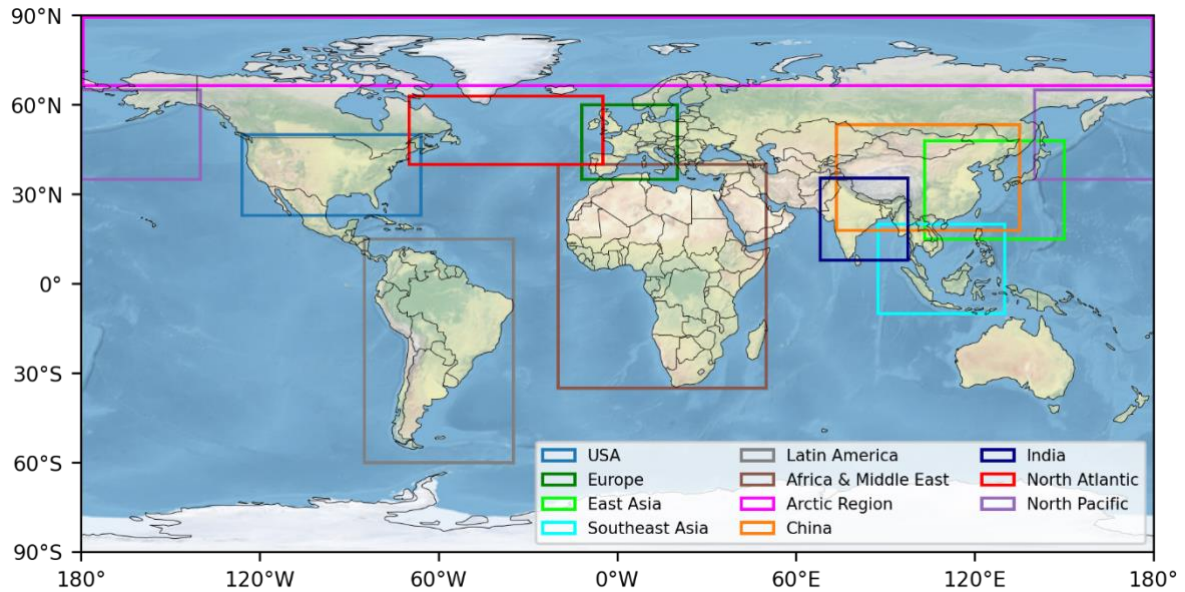
- 254 • **contrail waypoint outputs**, which includes the local meteorology and simulated
- 255 contrail properties at each contrail waypoint and provided at time steps of dt (300 s)
- 256 from their formation to end of life,
- 257 • **flight waypoint outputs**, where the contrail waypoint outputs are aggregated back to
- 258 the original flight waypoints,
- 259 • **flight level outputs**, where the flight waypoint outputs are aggregated for each flight,
- 260 • **time slice outputs**, where the contrail and flight waypoint outputs are summarised at
- 261 time steps of 1 h, and
- 262 • **gridded outputs**, where the contrail and flight waypoint outputs are aggregated to a
- 263 grid with a $0.5^\circ \times 0.5^\circ$ horizontal resolution and at a 1 h temporal resolution.

264 In this study, we use the: (i) flight level and time slice outputs to derive the annual and seasonal
 265 statistics; (ii) gridded outputs to estimate the regional air traffic and contrail properties, where
 266 the spatial bounding boxes that defines each region were used in previous studies (Wilkerson
 267 et al., 2010; Country bounding boxes, 2022; Teoh et al., 2023) and reproduced in Table S5 and
 268 Fig. S7; and (iii) contrail waypoint outputs to identify the set of conditions that produces
 269 strongly warming/cooling contrail segments.

270 **Table S5: Spatial bounding boxes used to estimate the regional air traffic, emissions, and contrail**
 271 **properties.**

| Region | Bounding box | | | | Surface area ($\times 10^{13} \text{ m}^2$) | Global surface area* |
|----------------------|--------------|----------|----------|----------|--|----------------------|
| USA | (126° W, | 23° N, | 66° W, | 50° N) | 1.6005 | 3.1% |
| Europe | (12° W, | 35° N, | 20° E, | 60° N) | 0.6662 | 1.3% |
| East Asia | (103° E, | 15° N, | 150° E, | 48° N) | 1.6170 | 3.2% |
| Southeast Asia | (87.5° E, | 10° S, | 130° E, | 20° N) | 1.5533 | 3.1% |
| Latin America | (85° W, | 60° S, | 35° W, | 15° N) | 3.9774 | 7.8% |
| Africa & Middle East | (20° W, | 35° S, | 50° E, | 40° N) | 6.0334 | 12% |
| China | (73.5° E, | 18° N, | 135° E, | 53.5° N) | 2.1628 | 4.2% |
| India | (68° E, | 8° N, | 97.5° E, | 35.5° N) | 0.9244 | 1.8% |
| North Atlantic | (70° W, | 40° N, | 5° W, | 63° N) | 1.1493 | 2.3% |
| North Pacific | (140° E, | 35° N, | 120° W, | 65° N) | 2.3577 | 4.6% |
| Arctic Region | (180° W, | 66.5° N, | 180° E, | 90° N) | 2.1548 | 4.2% |

272 * There are some overlapping between regional bounding boxes (Fig. S7), and therefore, the summation of
 273 regional statistics does not add up to 100%.

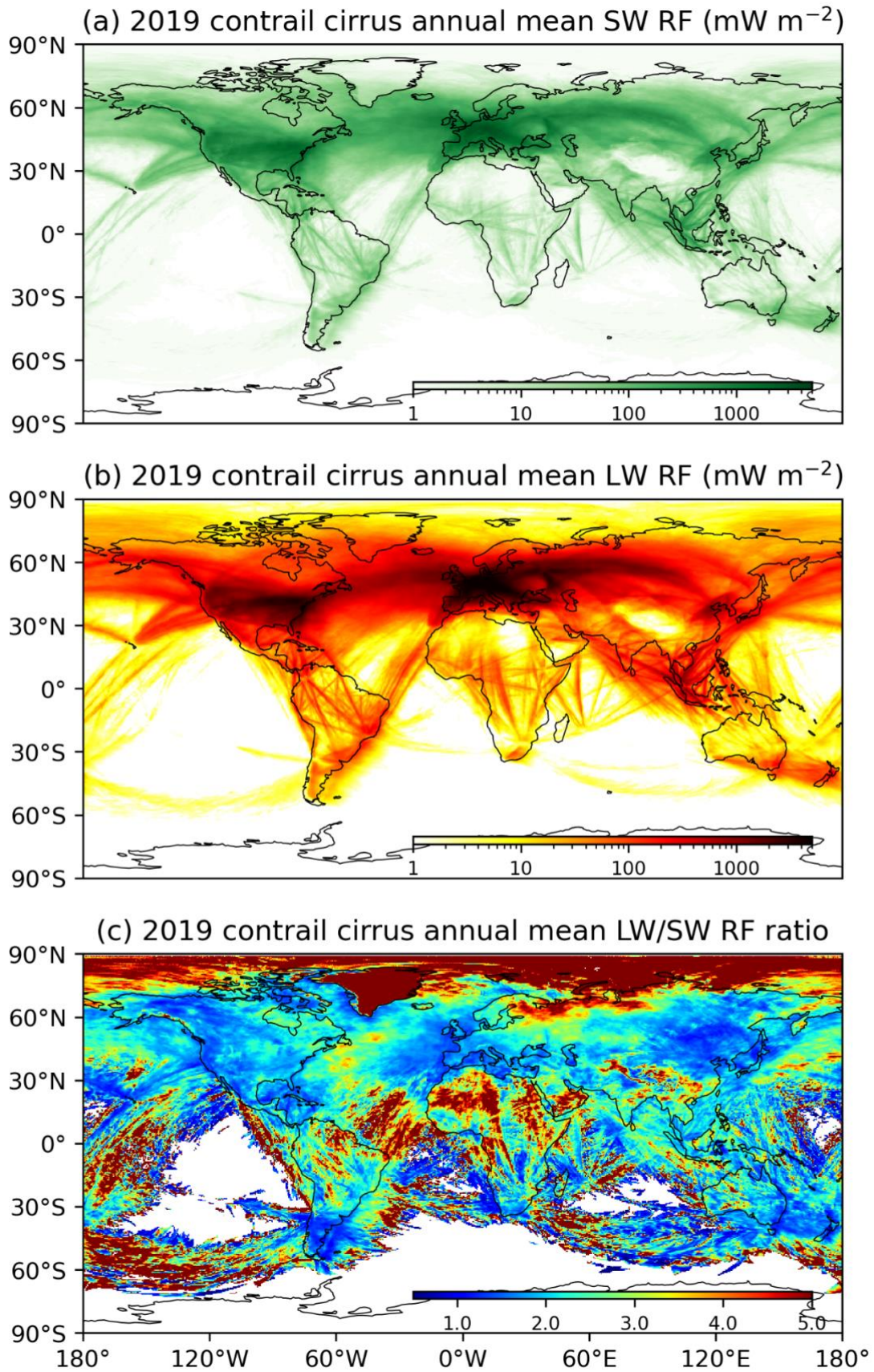


274

275 **Figure S7: Spatial bounding box used to estimate the regional air traffic, emissions, and contrail properties.**
 276 **The specific dimensions of these bounding boxes can be found in Table S5. Basemap plotted using Cartopy**
 277 **0.21.1 © Natural Earth; license: public domain.**

278 **S3 Global contrail simulation**

279 The global annual mean contrail cirrus net RF is estimated to be 62.1 mW m⁻² in 2019, 27.3
 280 mW m⁻² in 2020, and 31.7 mW m⁻² in 2021 with significant regional variabilities. Table 2 in
 281 the main text summarises the regional air traffic, emissions, and contrail statistics for 2019,
 282 while Tables S6 and S7 presents the same regional statistics for 2020 and 2021. Fig. 1a in the
 283 main text shows the global annual mean contrail cirrus net RF, while Fig. S8 shows the global
 284 annual mean contrail SW and LW RF and estimates the ratio of contrail LW-to-SW RF. One
 285 of the factors contributing to variability in the regional annual mean contrail net RF is the
 286 differences in air traffic patterns. Fig. S9 shows that: (i) flights over the North Atlantic are
 287 predominantly flown at cruising altitudes, which likely led to a larger percentage of flight
 288 distance forming persistent contrails (p_{contrail}); while (ii) flights in the Chinese airspace are
 289 generally flown at lower cruising altitudes, which could contribute to a smaller p_{contrail} .



290

291 **Figure S8: The 2019 global annual mean contrail cirrus: (a) SW RF; (b) LW RF; and (c) the ratio of LW-**
 292 **to-SW RF. Basemap plotted using Cartopy 0.21.1 © Natural Earth; license: public domain.**

Table S6: Regional air traffic activity, emissions, and contrail properties for 2020.

| Regional statistics: 2020 | Global | USA | Europe | East Asia | SEA | Latin America | Africa & Middle East | China | India | North Atlantic | North Pacific | Arctic Region |
|---|---------|--------|--------|-----------|--------|---------------|----------------------|--------|--------|----------------|---------------|---------------|
| Annual distance flown ($\times 10^9$ km) | 34.50 | 11.27 | 3.592 | 6.298 | 1.569 | 1.071 | 2.015 | 6.848 | 1.257 | 1.159 | 1.615 | 0.1600 |
| - Percentage relative to global values ^a | - | 32.7% | 10.4% | 18.3% | 4.5% | 3.1% | 5.8% | 19.8% | 3.6% | 3.4% | 4.7% | 0.5% |
| Annual dist. flown above FL250 ($\times 10^9$ km) | 26.33 | 7.84 | 2.742 | 4.372 | 1.227 | 0.852 | 1.714 | 4.846 | 1.040 | 1.111 | 1.352 | 0.1513 |
| - Percentage relative to global values ^a | - | 29.8% | 10.4% | 16.6% | 4.7% | 3.2% | 6.5% | 18.4% | 3.9% | 4.2% | 5.1% | 0.6% |
| Air traffic density ($\text{km}^{-1} \text{h}^{-1}$) | 0.008 | 0.080 | 0.062 | 0.044 | 0.012 | 0.003 | 0.004 | 0.036 | 0.016 | 0.012 | 0.008 | 0.001 |
| Fuel burn (Tg) | 146.000 | 32.400 | 14.600 | 29.500 | 7.730 | 4.450 | 9.910 | 31.600 | 6.200 | 6.830 | 10.800 | 1.140 |
| Mean nvPM EI _n ($\times 10^{15} \text{kg}^{-1}$) | 1.016 | 1.328 | 1.085 | 1.136 | 0.913 | 0.954 | 0.810 | 1.149 | 1.010 | 0.569 | 0.646 | 0.413 |
| Mean nvPM per dist. ($\times 10^{12} \text{m}^{-1}$) | 4.265 | 3.82 | 4.41 | 5.32 | 4.50 | 3.96 | 3.98 | 5.30 | 4.98 | 3.36 | 4.32 | 2.95 |
| Persistent contrail length ($\times 10^9$ km) | 1.40 | 0.429 | 0.237 | 0.0700 | 0.0618 | 0.0357 | 0.0493 | 0.0907 | 0.0215 | 0.107 | 0.0805 | 0.0193 |
| - Percentage relative to global values ^a | - | 30.6% | 16.9% | 5.0% | 4.4% | 2.5% | 3.5% | 6.5% | 1.5% | 7.6% | 5.7% | 1.4% |
| Dist. forming persistent contrails | 4.07% | 3.81% | 6.60% | 1.11% | 3.94% | 3.33% | 2.45% | 1.32% | 1.71% | 9.2% | 4.98% | 12.06% |
| Area-mean contrail optical depth, τ | 0.014 | 0.043 | 0.049 | 0.020 | 0.014 | 0.012 | 0.011 | 0.020 | 0.015 | 0.027 | 0.020 | 0.023 |
| Mean contrail age in domain (h) | 2.34 | 1.97 | 2.01 | 2.46 | 2.98 | 3.04 | 2.66 | 2.48 | 2.58 | 2.36 | 2.64 | 3.98 |
| Contrail cirrus coverage (%) | 0.03 | 0.18 | 0.43 | 0.02 | 0.01 | 0.003 | 0.01 | 0.05 | 0.01 | 0.12 | 0.04 | 0.03 |
| Contrail cirrus coverage, clear sky (%) | 0.28 | 2.7 | 3.6 | 0.43 | 0.24 | 0.03 | 0.04 | 0.41 | 0.11 | 1.1 | 0.28 | 0.09 |
| Annual mean SW RF (mW m^{-2}) | -26.4 | -241 | -359 | -40.1 | -38.9 | -6.54 | -7.74 | -42.7 | -19.1 | -77.2 | -29.0 | -3.69 |
| Annual mean LW RF (mW m^{-2}) | 53.8 | 444 | 699 | 69.5 | 72.8 | 15.0 | 14.9 | 73.9 | 41.8 | 181 | 56.8 | 20.6 |
| Annual mean Net RF (mW m^{-2}) | 27.3 | 203 | 339 | 29.3 | 33.8 | 8.42 | 7.15 | 31.2 | 22.6 | 104 | 27.7 | 17.0 |
| Ratio: LW/SW RF | 2.04 | 1.84 | 1.95 | 1.73 | 1.87 | 2.29 | 1.93 | 1.73 | 2.19 | 2.34 | 1.96 | 5.58 |
| EF _{contrail} ($\times 10^{18} \text{J}$) | 441 | 103 | 71.4 | 15.0 | 16.6 | 10.6 | 13.6 | 21.3 | 6.61 | 37.6 | 20.8 | 11.6 |
| - Percentage relative to global values ^a | - | 23.4% | 16.2% | 3.4% | 3.8% | 2.4% | 3.1% | 4.8% | 1.5% | 8.5% | 4.7% | 2.6% |
| EF _{contrail, initial location} ($\times 10^{18} \text{J}$) ^b | 441 | 106 | 79.4 | 15.0 | 16.8 | 10.7 | 13.7 | 20.2 | 6.41 | 39.3 | 21.1 | 9.18 |
| - Percentage relative to global values ^a | - | 24.0% | 18.0% | 3.4% | 3.8% | 2.4% | 3.1% | 4.6% | 1.5% | 8.9% | 4.8% | 2.1% |
| Ratio: EF _{contrail} /EF _{contrail, initial} ^c | 1.00 | 0.97 | 0.90 | 1.00 | 0.99 | 0.99 | 0.99 | 1.05 | 1.03 | 0.96 | 0.99 | 1.26 |
| EF _{contrail} per flight distance ($\times 10^8 \text{J m}^{-1}$) | 0.128 | 0.094 | 0.221 | 0.024 | 0.107 | 0.100 | 0.068 | 0.029 | 0.051 | 0.339 | 0.131 | 0.574 |
| EF _{contrail} per contrail length ($\times 10^8 \text{J m}^{-1}$) | 3.14 | 2.47 | 3.35 | 2.14 | 2.72 | 3.00 | 2.78 | 2.23 | 2.98 | 3.67 | 2.62 | 4.76 |

294 ^a: There are some overlapping between regional bounding boxes (Fig. S7), and therefore, the summation of regional statistics does not add up to 100%.

295 ^b: The total EF_{contrail} throughout the contrail lifetime is added back to the location where contrails were initially formed.

296 ^c: A higher ratio indicates that a larger share of contrail climate forcing is from contrails initially formed outside of the region but subsequently advected into the domain.

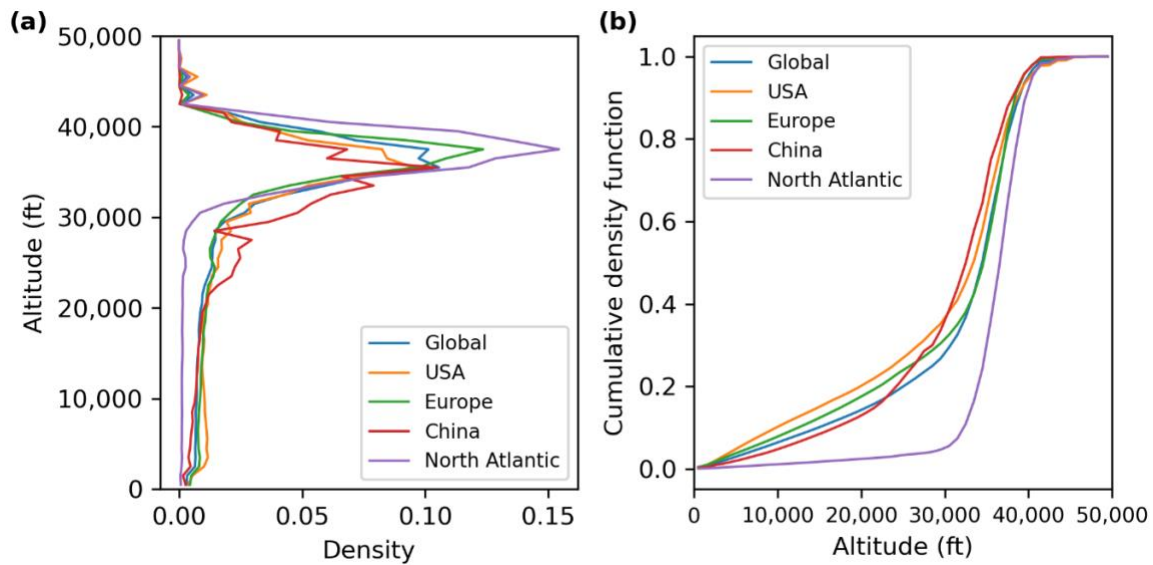
297 **Table S7: Regional air traffic activity, emissions, and contrail properties for 2021.**

| Regional statistics: 2021 | Global | USA | Europe | East Asia | SEA | Latin America | Africa & Middle East | China | India | North Atlantic | North Pacific | Arctic Region |
|---|---------|--------|--------|-----------|--------|---------------|----------------------|--------|--------|----------------|---------------|---------------|
| Annual distance flown ($\times 10^9$ km) | 41.90 | 15.17 | 4.475 | 5.948 | 1.208 | 1.479 | 2.795 | 6.654 | 1.438 | 1.441 | 1.741 | 0.1930 |
| - Percentage relative to global values ^a | - | 36.2% | 10.7% | 14.2% | 2.9% | 3.5% | 6.7% | 15.9% | 3.4% | 3.4% | 4.2% | 0.5% |
| Annual dist. flown above FL250 ($\times 10^9$ km) | 31.70 | 10.40 | 3.432 | 4.089 | 0.995 | 1.143 | 2.343 | 4.694 | 1.158 | 1.382 | 1.445 | 0.1791 |
| - Percentage relative to global values ^a | - | 32.8% | 10.8% | 12.9% | 3.1% | 3.6% | 7.4% | 14.8% | 3.7% | 4.4% | 4.6% | 0.6% |
| Air traffic density ($\text{km}^{-1} \text{h}^{-1}$) | 0.009 | 0.108 | 0.077 | 0.042 | 0.009 | 0.004 | 0.005 | 0.035 | 0.018 | 0.014 | 0.008 | 0.001 |
| Fuel burn (Tg) | 166.000 | 42.500 | 16.800 | 27.800 | 6.140 | 5.640 | 12.590 | 30.200 | 6.390 | 8.350 | 11.500 | 1.330 |
| Mean nvPM EI _n ($\times 10^{15} \text{kg}^{-1}$) | 1.021 | 1.317 | 1.061 | 1.088 | 0.774 | 0.950 | 0.817 | 1.116 | 1.024 | 0.540 | 0.604 | 0.381 |
| Mean nvPM per dist. ($\times 10^{12} \text{m}^{-1}$) | 4.009 | 3.69 | 3.98 | 5.09 | 3.93 | 3.62 | 3.68 | 5.06 | 4.55 | 3.13 | 3.99 | 2.62 |
| Persistent contrail length ($\times 10^9$ km) | 1.73 | 0.538 | 0.266 | 0.0813 | 0.0753 | 0.0568 | 0.0721 | 0.104 | 0.0328 | 0.137 | 0.1000 | 0.0140 |
| - Percentage relative to global values ^a | - | 31.1% | 15.4% | 4.7% | 4.3% | 3.3% | 4.2% | 6.0% | 1.9% | 7.9% | 5.8% | 0.8% |
| Dist. forming persistent contrails | 4.13% | 3.55% | 5.94% | 1.37% | 6.23% | 3.84% | 2.58% | 1.56% | 2.28% | 9.5% | 5.74% | 7.26% |
| Area-mean contrail optical depth, τ | 0.012 | 0.046 | 0.046 | 0.021 | 0.014 | 0.012 | 0.010 | 0.020 | 0.015 | 0.027 | 0.021 | 0.022 |
| Mean contrail age in domain (h) | 2.25 | 1.91 | 1.93 | 2.47 | 3.06 | 3.16 | 2.55 | 2.48 | 2.56 | 2.35 | 2.62 | 3.72 |
| Contrail cirrus coverage (%) | 0.04 | 0.21 | 0.55 | 0.02 | 0.01 | 0.006 | 0.01 | 0.05 | 0.01 | 0.20 | 0.05 | 0.02 |
| Contrail cirrus coverage, clear sky (%) | 0.33 | 3.3 | 3.9 | 0.52 | 0.26 | 0.06 | 0.06 | 0.50 | 0.19 | 1.2 | 0.37 | 0.04 |
| Annual mean SW RF (mW m^{-2}) | -33.0 | -304 | -420 | -47.8 | -45.1 | -10.0 | -9.95 | -50.5 | -27.3 | -104 | -36.6 | -4.18 |
| Annual mean LW RF (mW m^{-2}) | 64.8 | 545 | 773 | 79.2 | 86.3 | 22.8 | 19.8 | 85.2 | 60.6 | 234 | 70.7 | 13.7 |
| Annual mean Net RF (mW m^{-2}) | 31.7 | 240 | 352 | 31.3 | 41.1 | 12.8 | 9.79 | 34.7 | 33.2 | 130 | 34.0 | 9.56 |
| Ratio: LW/SW RF | 1.96 | 1.79 | 1.84 | 1.66 | 1.91 | 2.28 | 1.99 | 1.69 | 2.22 | 2.25 | 1.93 | 3.28 |
| EF _{contrail} ($\times 10^{18} \text{J}$) | 511 | 121 | 74 | 15.9 | 20.1 | 16 | 18.6 | 23.6 | 9.67 | 47.1 | 25.4 | 6.51 |
| - Percentage relative to global values ^a | - | 23.7% | 14.5% | 3.1% | 3.9% | 3.1% | 3.6% | 4.6% | 1.9% | 9.2% | 5.0% | 1.3% |
| EF _{contrail, initial location} ($\times 10^{18} \text{J}$) ^b | 511 | 125 | 77.2 | 16.1 | 20.3 | 16.5 | 19.5 | 21.8 | 9.63 | 48.7 | 25.3 | 5.26 |
| - Percentage relative to global values ^a | - | 24.5% | 15.1% | 3.2% | 4.0% | 3.2% | 3.8% | 4.3% | 1.9% | 9.5% | 5.0% | 1.0% |
| Ratio: EF _{contrail} /EF _{contrail, initial} ^c | 1.00 | 0.97 | 0.96 | 0.99 | 0.99 | 0.97 | 0.95 | 1.08 | 1.00 | 0.97 | 1.00 | 1.24 |
| EF _{contrail} per flight distance ($\times 10^8 \text{J m}^{-1}$) | 0.122 | 0.082 | 0.173 | 0.027 | 0.168 | 0.112 | 0.070 | 0.033 | 0.067 | 0.338 | 0.145 | 0.273 |
| EF _{contrail} per contrail length ($\times 10^8 \text{J m}^{-1}$) | 2.95 | 2.32 | 2.90 | 1.98 | 2.70 | 2.90 | 2.70 | 2.10 | 2.94 | 3.55 | 2.53 | 3.76 |

298 ^a: There are some overlapping between regional bounding boxes (Fig. S7), and therefore, the summation of regional statistics does not add up to 100%.

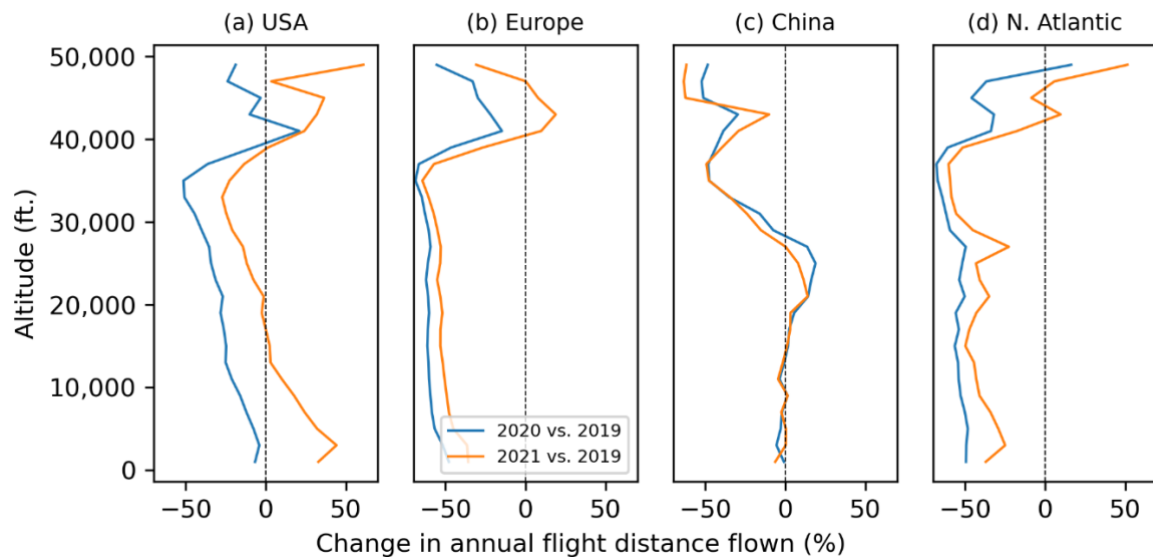
299 ^b: The total EF_{contrail} throughout the contrail lifetime is added back to the location where contrails were initially formed.

300 ^c: A higher ratio indicates that a larger share of contrail climate forcing is from contrails initially formed outside of the region but subsequently advected into the domain.



301

302 **Figure S9: The (a) probability density function and (b) cumulative density function of the 2019 annual flight**
 303 **distance flown across the globe (blue lines) and over the USA (orange lines), Europe (green lines), China**
 304 **(red lines) and the North Atlantic (purple lines).**

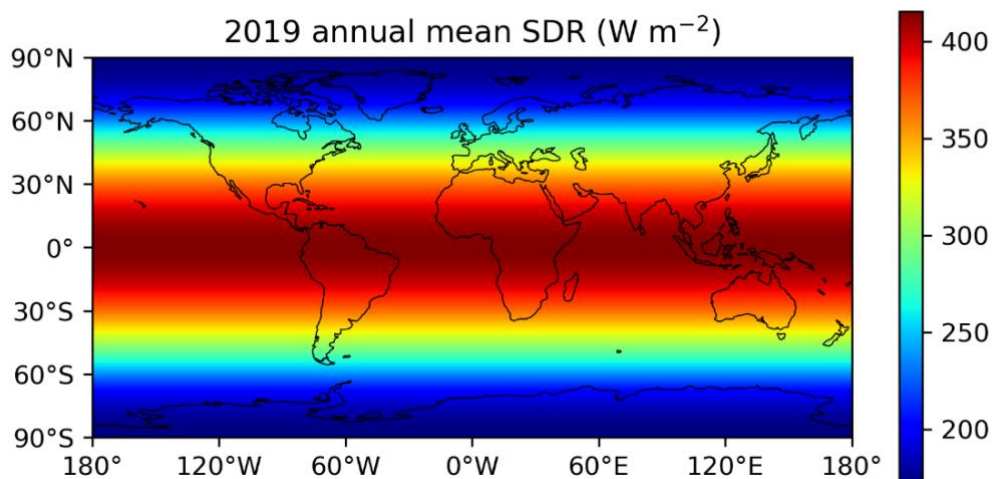


305

306 **Figure S10: The percentage change in annual flight distance flown by altitude over the (a) USA; (b) Europe;**
 307 **(c) China; and (d) North Atlantic when comparing the air traffic in 2019 versus 2020 (blue lines) and 2021**
 308 **(orange lines).**

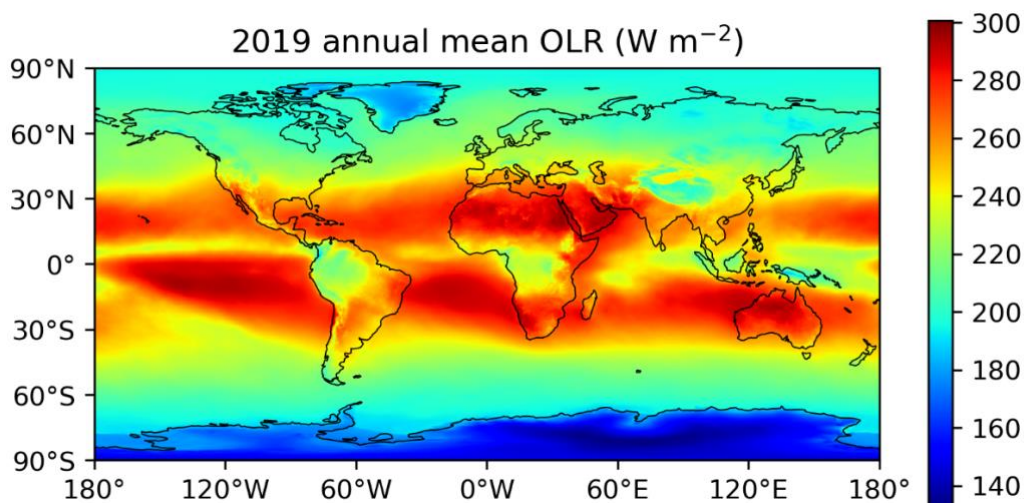
309 Over the USA, Europe and North Atlantic, Fig. S10 shows that the COVID-19 pandemic led
 310 to significant reductions in air traffic activity between 20,000 and 40,000 feet, but there are
 311 only small changes in air traffic activity above 40,000 feet, likely due to a higher share of
 312 private business jets (ICAO, 2021; Sobieralski and Mumbower, 2022). The reduction in annual
 313 mean contrail net RF in East Asia and China (50 – 54%) is significantly larger than the change
 314 in flight distance flown (-24%), and this is most likely due to the: (i) lower share of international

315 overflights which led to a 39% reduction in air traffic activity above 30,000 feet; and (ii) higher
316 share of domestic air traffic in parts of China (Fig. 4a in the main text) that caused an 8%
317 increase in flight distance flown between 25,000 and 30,000 feet (Fig. S10c) where persistent
318 contrail formation is less likely.



319
320 **Figure S11: The 2019 global annual mean solar direct radiation that is provided by the ERA5 HRES.**
321 **Basemap plotted using Cartopy 0.21.1 © Natural Earth; license: public domain.**

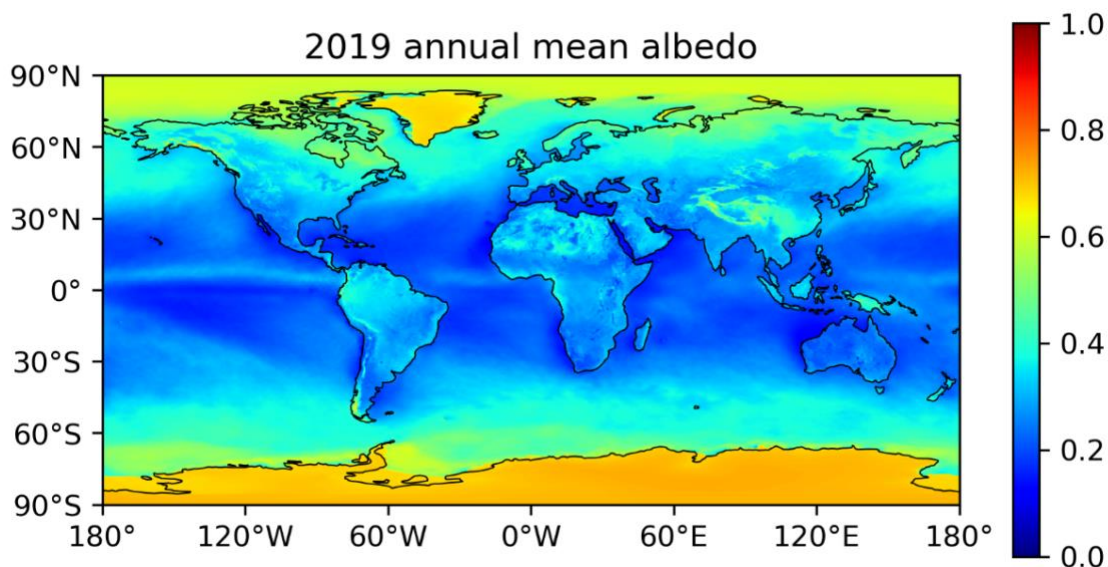
322



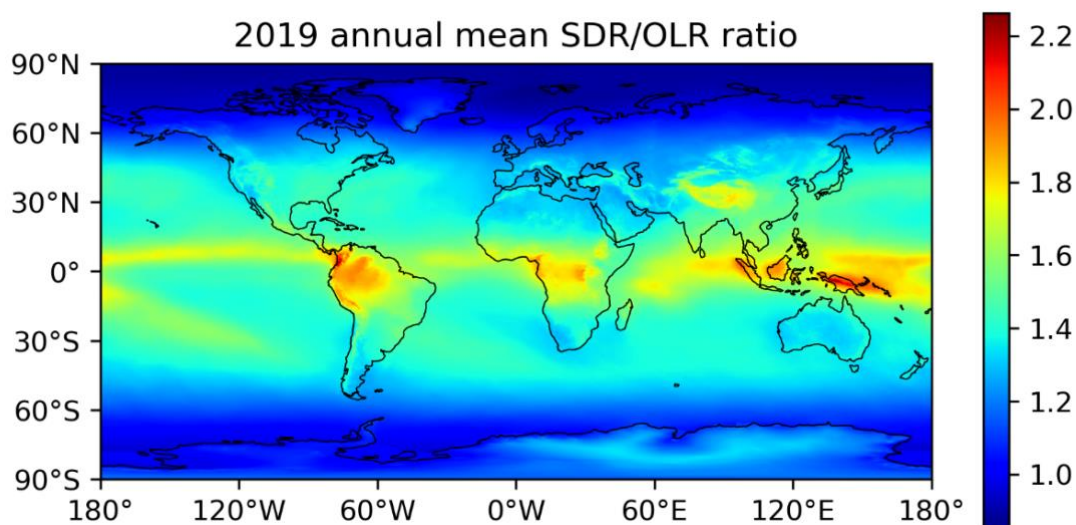
323
324 **Figure S12: The 2019 global annual mean outgoing longwave radiation that is provided by the ERA5**
325 **HRES. Basemap plotted using Cartopy 0.21.1 © Natural Earth; license: public domain.**

326 The solar direct radiation (SDR) and effective albedo, the proportion of solar radiation reflected
327 by the surface and natural cirrus and calculated by dividing the reflected solar radiation (RSR)
328 with the SDR, impact the contrail shortwave (SW) RF; while the magnitude of outgoing

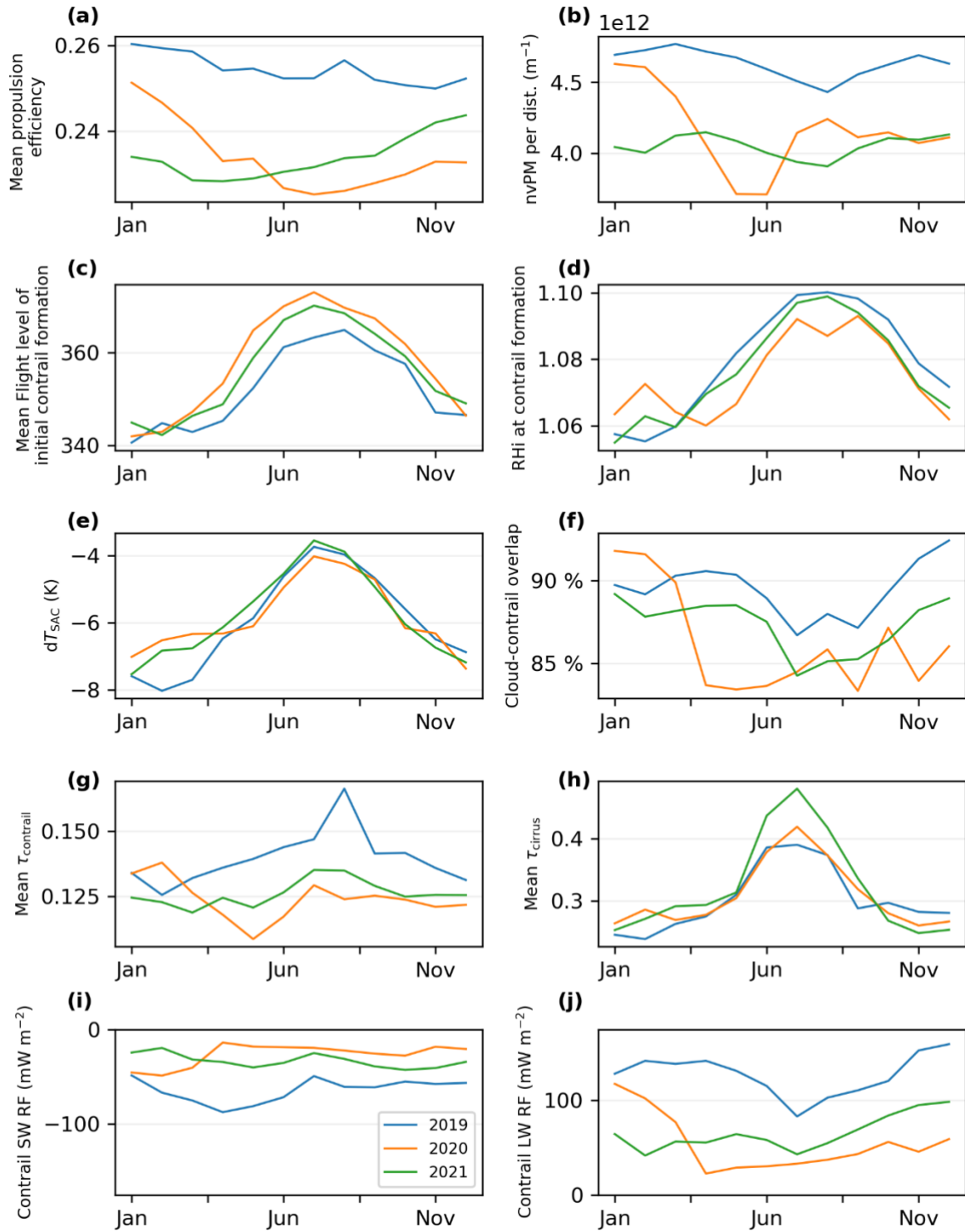
329 longwave radiation (OLR) influences the contrail longwave (LW) RF. Fig. S11 to S14 shows
 330 the spatial variations in global annual mean SDR, OLR, effective albedo, and the ratio of SDR-
 331 to-OLR, where: (i) the subtropics and Sahara Desert tends to have a high relative OLR (Fig.
 332 S12); (ii) the Arctic, Greenland and Antarctica have the highest effective albedo (Fig. S13);
 333 and (iii) Southeast Asia have the highest ratio of SDR-to-OLR (Fig. S14) which leads to a
 334 higher probability of forming strongly cooling contrails.



335
 336 **Figure S13: The 2019 global annual mean surface and cloud albedo as derived by dividing the annual mean**
 337 **reflected solar radiation by the solar direct radiation at each grid cell. Basemap plotted using Cartopy**
 338 **0.21.1 © Natural Earth; license: public domain.**



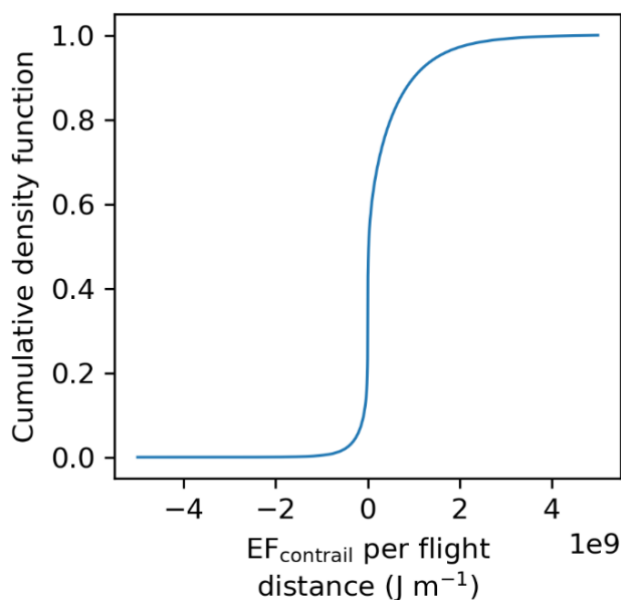
339
 340 **Figure S14: The ratio of the annual mean solar direct radiation (SDR) to the annual mean outgoing**
 341 **longwave radiation (OLR) for 2019, where the SDR and OLR are provided by the ERA5 HRES. Basemap**
 342 **plotted using Cartopy 0.21.1 © Natural Earth; license: public domain.**



343

344 **Figure S15: Monthly statistics on the: (a) global fleet-aggregated mean overall propulsion efficiency and**
 345 **(b) nvPM per flight distance flown; mean (c) flight level, (d) RHi, and (e) difference in the ambient**
 346 **temperature and Schmidt-Appleman criterion threshold temperature (dT_{SAC}) where contrails were initially**
 347 **formed; (f) mean percentage of cloud-contrail overlap; the lifetime mean (g) contrail optical depth**
 348 **($\tau_{contrail}$) and (h) overlying natural cirrus optical depth (τ_{cirrus}); and the global annual mean contrail (i)**
 349 **SW RF and (j) LW RF.**

350 Fig. 5 in the main text and Fig. S15 summarises the seasonal variations in: (i) global annual
 351 flight distance flown; (ii) meteorological conditions where persistent contrails were initially
 352 formed; fleet-aggregated (iii) non-volatile particulate matter (nvPM) emissions; (iv) fraction of
 353 nvPM that formed ice crystals in persistent contrails; (v) mean contrail properties, such as the
 354 volume-mean ice crystal radius (r_{ice}), optical depth ($\tau_{contrail}$), lifetime, coverage area, and
 355 cloud-contrail overlap; and (vi) their associated RF and energy forcing ($EF_{contrail}$) per unit
 356 length of contrail.



357
 358 **Figure S16: Cumulative density function of the magnitude of $EF_{contrail}$ per flight distance flown for every**
 359 **flight segment that formed persistent contrails in 2019. The percentiles of the $EF_{contrail}$ per flight distance is**
 360 **presented in Table S8.**

361

362 **Table S8: The threshold of $EF_{contrail}$ per flight distance flown by percentile.**

| Percentile | $EF_{contrail}$ per flight distance ($J m^{-1}$) |
|------------------|--|
| 1 st | -7.11×10^8 |
| 5 th | -2.39×10^8 |
| 33 rd | 1.00×10^6 |
| 50 th | 1.90×10^7 |
| 68 th | 1.97×10^8 |
| 95 th | 1.54×10^9 |
| 99 th | 2.85×10^9 |

363 Fig. S16 presents the cumulative density function of the EF_{contrail} per flight distance flown for
364 flight segments that formed persistent contrails in 2019. As every flight segment formed
365 persistent contrails and the initial contrail length is equal to the flight segment length, the
366 EF_{contrail} per flight distance is expected to have the same magnitude as EF_{contrail} per persistent
367 contrail length. We use this data to define strongly warming contrail segments as those with
368 EF_{contrail} per contrail length greater than the 95th percentile ($> 15.4 \times 10^8 \text{ J m}^{-1}$), while strongly
369 cooling contrail segments have an EF_{contrail} per contrail length below the 5th percentile (< -2.39
370 $\times 10^8 \text{ J m}^{-1}$). Fig. 7a in the main text shows that the most strongly warming contrail segments
371 are more prevalent over the US and North Atlantic, and Table S9 suggests that these contrail
372 segments are generally formed by: (i) eastbound transatlantic flights from the North/South
373 America to Europe and; (ii) transcontinental flights across the US, likely because these routes
374 generally depart during the evenings (Teoh et al., 2022). In contrast, the most strongly cooling
375 contrail segments are more common over Southeast Asia, Northern Asia, Europe, and the east
376 of the North Atlantic (Fig. 7b in the main text) and Table S10 suggests that these contrails are
377 formed by: (i) short-/medium-haul flights around Southeast and East Asia, likely because the
378 region has a highest ratio of SDR to OLR relative to other regions; long-haul flights (ii) from
379 the Middle East to Southeast Asia/Oceania and (iii) from Asia to Europe, likely due to flight
380 scheduling factors where they have a higher probability of forming persistent contrails around
381 dawn before they arrive to their destination; and (iv) westbound transatlantic air traffic activity
382 that is generally highest during the morning (Teoh et al., 2022). Tables S9 and S10 also show
383 that the top 20 origin-destination airport pairs accounted for: (i) 5.5% of the flights that formed
384 strongly warming contrail segments; and (ii) 8.3% of the flights that formed strongly cooling
385 contrail segments.

386 **Table S9: Top 20 origin-destination airport pairs that contribute to the strongly warming contrail segments**
 387 **(EF_{contrail} per contrail length $> 15.4 \times 10^8 \text{ J m}^{-1}$, 95th percentile) that were presented in Fig. 7 in the main text.**

| | Origin Airport | Destination Airport | % of flights* |
|----|--|--|---------------|
| 1 | John F Kennedy International Airport | London Heathrow Airport | 0.65 |
| 2 | Los Angeles International Airport | John F Kennedy International Airport | 0.42 |
| 3 | Washington Dulles International Airport | London Heathrow Airport | 0.38 |
| 4 | Ted Stevens Anchorage International Airport | Louisville Muhammad Ali International Airport | 0.33 |
| 5 | John F Kennedy International Airport | Los Angeles International Airport | 0.32 |
| 6 | San Francisco International Airport | John F Kennedy International Airport | 0.30 |
| 7 | Pointe-à-Pitre Le Raizet International Airport | Paris-Orly Airport | 0.29 |
| 8 | John F Kennedy International Airport | Adolfo Suárez Madrid-Barajas Airport | 0.25 |
| 9 | John F Kennedy International Airport | Charles de Gaulle International Airport | 0.24 |
| 10 | Orlando International Airport | London Gatwick Airport | 0.23 |
| 11 | Newark Liberty International Airport | London Heathrow Airport | 0.23 |
| 12 | Logan International Airport | Seattle Tacoma International Airport | 0.22 |
| 13 | Philadelphia International Airport | London Heathrow Airport | 0.22 |
| 14 | San Francisco International Airport | London Heathrow Airport | 0.21 |
| 15 | Adolfo Suárez Madrid-Barajas Airport | Licenciado Benito Juárez International Airport | 0.21 |
| 16 | Miami International Airport | London Heathrow Airport | 0.21 |
| 17 | Miami International Airport | Charles de Gaulle International Airport | 0.20 |
| 18 | Logan International Airport | Denver International Airport | 0.20 |
| 19 | Hartsfield Jackson Atlanta International Airport | Rome-Fiumicino Leonardo da Vinci International Airport | 0.20 |
| 20 | John F Kennedy International Airport | Malpensa International Airport | 0.20 |

* Percentage of the subset of flights that formed strongly warming contrail segments

388

389 **Table S10: Top 20 origin-destination airport pairs that contribute to the strongly cooling contrail segments**
 390 **(EF_{contrail} per contrail length $< -2.39 \times 10^8 \text{ J m}^{-1}$, 5th percentile) that were presented in Fig. 7 in the main text.**

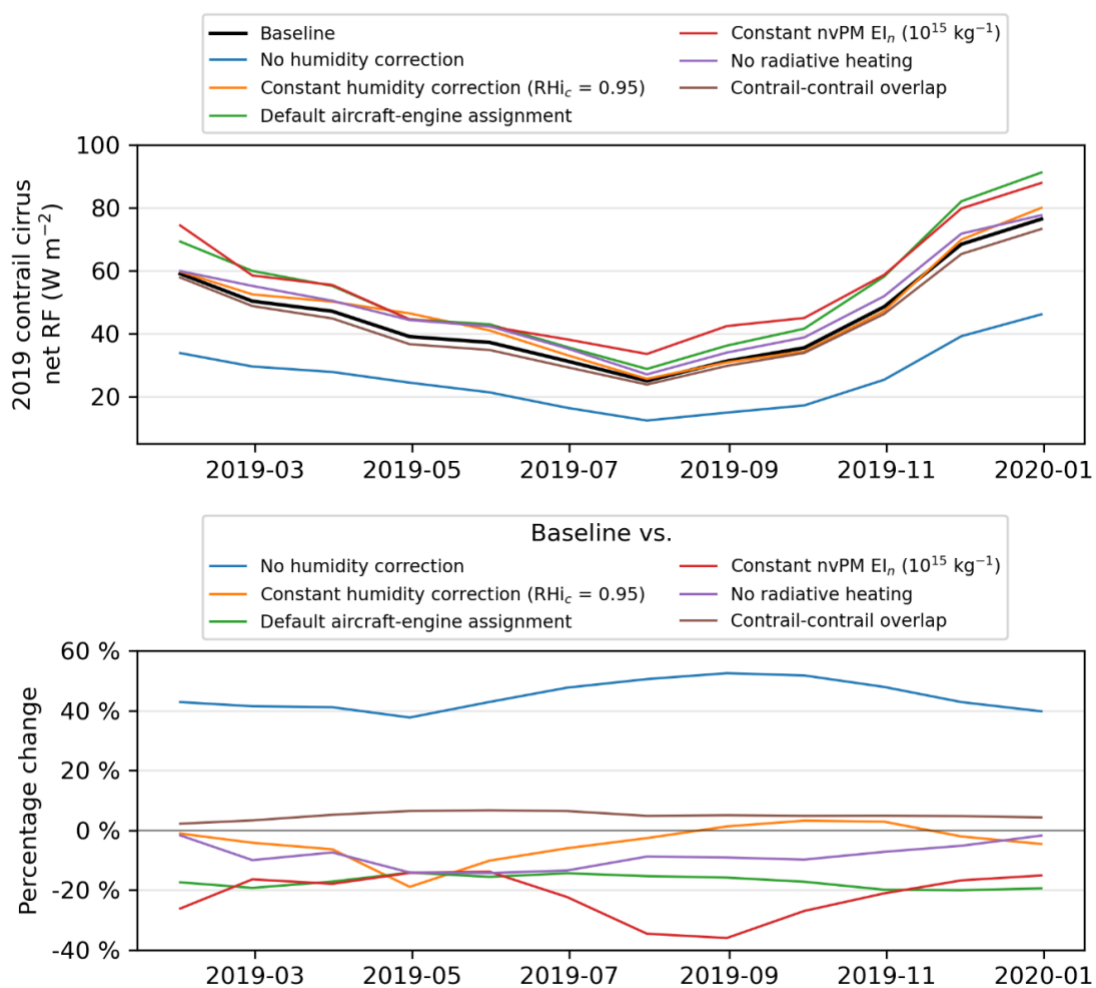
| | Origin Airport | Destination Airport | % of flights* |
|----|--|---|---------------|
| 1 | Singapore Changi Airport | Suvarnabhumi Airport | 0.61 |
| 2 | Abu Dhabi International Airport | Soekarno-Hatta International Airport | 0.54 |
| 3 | Soekarno-Hatta International Airport | Narita International Airport | 0.51 |
| 4 | Singapore Changi Airport | Hong Kong International Airport | 0.47 |
| 5 | Dubai International Airport | Dallas Fort Worth International Airport | 0.47 |
| 6 | Sydney Kingsford Smith International Airport | Suvarnabhumi Airport | 0.47 |
| 7 | Brisbane International Airport | Singapore Changi Airport | 0.46 |
| 8 | Dubai International Airport | John F Kennedy International Airport | 0.46 |
| 9 | Dubai International Airport | Singapore Changi Airport | 0.44 |
| 10 | Dubai International Airport | Perth International Airport | 0.43 |
| 11 | Shanghai Pudong International Airport | Frankfurt am Main Airport | 0.38 |
| 12 | Dubai International Airport | Melbourne International Airport | 0.37 |
| 13 | Kuala Lumpur International Airport | Taiwan Taoyuan International Airport | 0.36 |
| 14 | Singapore Changi Airport | Brisbane International Airport | 0.36 |
| 15 | Kuala Lumpur International Airport | Soekarno-Hatta International Airport | 0.36 |
| 16 | Beijing Capital International Airport | Zürich Airport | 0.36 |
| 17 | Yuzhno-Sakhalinsk Airport | Novosibirsk Tolmachevo Airport | 0.33 |
| 18 | Sydney Kingsford Smith International Airport | Hong Kong International Airport | 0.32 |
| 19 | Soekarno-Hatta International Airport | Hong Kong International Airport | 0.32 |
| 20 | Incheon International Airport | Ninoy Aquino International Airport | 0.32 |

* Percentage of the subset of flights that formed strongly cooling contrail segments

391

392 **S4 Sensitivity analysis**

393 Table S11 summarises the sensitivity of the simulated contrail properties and climate forcing
 394 to the corrections applied to the ERA5 HRES humidity fields, assumptions in aircraft-engine
 395 assignment and emissions, and contrail model parameters. Fig. S17 presents the global monthly
 396 mean contrail net RF from the different simulation runs, and shows that the percentage change
 397 in global monthly contrail net RF exhibits seasonal effects when comparing between the
 398 baseline simulation versus the simulation: (i) without humidity correction; (ii) with a constant
 399 humidity correction, c.f. Eq. (S5) where $RH_{ic} = 0.95$; (iii) with a constant nvPM EI_n of 10^{15} kg^{-1}
 400 ¹ for all waypoints; and (iv) without radiative heating interactions with the contrail plume.



401
 402 **Figure S17: Comparison of the global monthly mean contrail net RF between the baseline scenario versus**
 403 **the simulation without humidity correction (blue lines), the simulation with default aircraft-engine**
 404 **assignments from BADA (orange lines), and the simulation without radiative heating effects (green lines).**

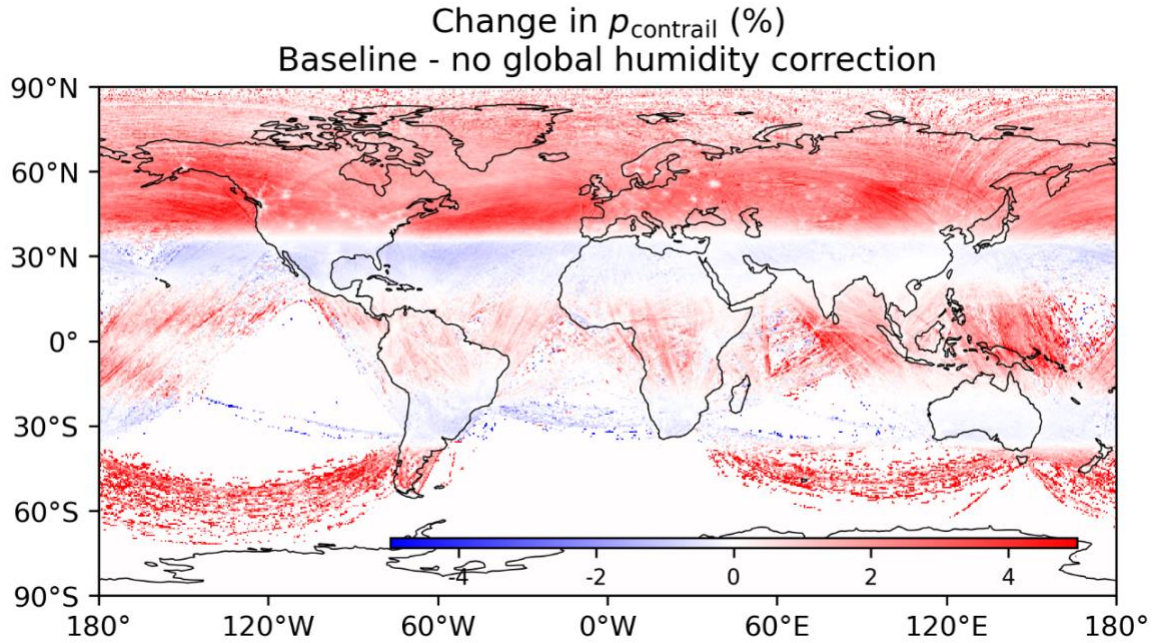
Table S11: The 2019 global annual aviation fuel consumption, emissions, and contrail properties from the different model runs used in the sensitivity analysis.

| 2019 sensitivity analysis | | Baseline | No humidity correction | Constant humidity correction (RHic = 0.95) | Default aircraft-engine: BADA | Constant nvPM EI _n (10 ¹⁵ kg ⁻¹) | Constant nvPM EI _n (10 ¹⁴ kg ⁻¹) | No radiative heating |
|---|-----------------------------------|-----------|------------------------|--|-------------------------------|--|--|----------------------|
| Annual fuel burn | 10 ⁹ kg | 280.1 | 280.1 | 280.1 | 279.2 | 280.1 | 280.1 | 280.1 |
| Fuel burn per distance | kg km ⁻¹ | 4.596 | 4.596 | 4.596 | 4.582 | 4.596 | 4.596 | 4.596 |
| Annual CO ₂ emissions | 10 ⁹ kg | 884.8 | 884.8 | 884.8 | 882 | 884.8 | 884.8 | 884.8 |
| Mean overall propulsion efficiency, η | - | 0.297 | 0.302 | 0.297 | 0.297 | 0.297 | 0.297 | 0.297 |
| Mean nvPM EI _n | 10 ¹⁵ kg ⁻¹ | 1.02 | 1.02 | 1.02 | 1.39 | 1 | 0.1 | 1.02 |
| Mean nvPM per distance travelled | 10 ¹² m ⁻¹ | 4.69 | 4.69 | 4.69 | 6.35 | 4.6 | 0.46 | 4.69 |
| Flights forming contrails | % | 42.53 | 42.13 | 42.56 | 42.58 | 42.53 | 42.53 | 42.53 |
| Flights forming persistent contrails | % | 23.78 | 21.88 | 24.92 | 23.79 | 23.78 | 23.82 | 23.88 |
| Annual contrail length | 10 ⁹ km | 21.35 | 21.25 | 21.45 | 21.37 | 21.35 | 21.35 | 21.35 |
| Flight dist. forming contrails | % | 35 | 34.9 | 35.2 | 35.1 | 35 | 35 | 35 |
| Annual persistent contrail length | 10 ⁹ km | 3.018 | 2.564 | 3.452 | 3.017 | 3.014 | 3.039 | 3.058 |
| Flight dist. forming persistent contrails | % | 4.95 | 4.21 | 5.66 | 4.95 | 4.95 | 4.99 | 5.02 |
| Initial mean ice particle number per contrail length, $n_{ice,initial}$ | 10 ¹² m ⁻¹ | 2.5 | 2.22 | 2.45 | 3.31 | 2.25 | 0.22 | 2.5 |
| Mean lifetime ice particle number per contrail length, n_{ice} | 10 ¹² m ⁻¹ | 1.88 | 1.86 | 1.91 | 2.47 | 1.72 | 0.18 | 1.97 |
| Mean contrail lifetime | h | 2.43 | 2.21 | 2.44 | 2.56 | 2.56 | 1.66 | 3 |
| Mean ice particle volume mean radius, r_{ice} | μ m | 9.96 | 7.82 | 9.12 | 9.19 | 9.03 | 14.1 | 8.5 |
| Mean contrail segment optical depth, $\tau_{contrail}$ | - | 0.139 | 0.094 | 0.118 | 0.154 | 0.141 | 0.07 | 0.111 |
| Mean contrail width | m | 9903 | 8507 | 9864 | 10586 | 10521 | 5713 | 6875 |
| Mean contrail depth | m | 803 | 698 | 773 | 819 | 823 | 719 | 475 |
| Contrail cirrus coverage | % | 0.06 | 0.03 | 0.07 | 0.07 | 0.08 | 0.02 | 0.10 |
| Contrail cirrus coverage, clear sky | % | 0.66 | 0.37 | 0.66 | 0.74 | 0.86 | 0.08 | 0.60 |
| Cloud-contrail overlap | % | 90.2 | 91.8 | 89.8 | 90.6 | 90.7 | 67.5 | 83.1 |
| Number of flights: warming contrails | - | 6,741,548 | 6,034,669 | 7,041,971 | 6,693,704 | 6,721,659 | 7,031,761 | 6,922,105 |
| Number of flights: cooling contrails | - | 2,821,562 | 2,765,116 | 2,981,694 | 2,873,810 | 2,840,726 | 2,550,238 | 2,681,120 |
| Ratio: warming-to-cooling contrails | - | 2.39 | 2.18 | 2.36 | 2.33 | 2.37 | 2.76 | 2.58 |
| Mean SW RF' | W m ⁻² | -4.15 | -2.95 | -3.72 | -4.55 | -4.19 | -2.12 | -3.49 |
| Mean LW RF' | W m ⁻² | 5.36 | 3.48 | 4.69 | 5.78 | 5.51 | 3.23 | 4.4 |
| Mean net RF' | W m ⁻² | 1.22 | 0.533 | 0.97 | 1.23 | 1.33 | 1.11 | 0.908 |
| Annual mean SW RF | mW m ⁻² | -63.7 | -36.1 | -67.1 | -74.5 | -74.4 | -13.5 | -65.9 |
| Annual mean LW RF | mW m ⁻² | 126 | 70.9 | 132 | 148 | 149 | 27.3 | 133 |
| Annual mean net RF | mW m ⁻² | 62.1 | 34.8 | 64.5 | 73.1 | 74.8 | 13.7 | 66.8 |
| Annual EF _{contrail} | 10 ¹⁸ J | 999 | 559 | 1038 | 1176 | 1204 | 221 | 1075 |
| EF _{contrail} per flight distance | 10 ⁸ J m ⁻¹ | 0.164 | 0.092 | 0.17 | 0.193 | 0.198 | 0.036 | 0.176 |
| EF _{contrail} per contrail length | 10 ⁸ J m ⁻¹ | 3.31 | 2.18 | 3.01 | 3.9 | 3.99 | 0.727 | 3.51 |
| Flights responsible for 80% EF _{contrail} | % | 2.68 | 2.23 | 2.89 | 2.81 | 2.66 | 2.65 | 2.92 |

406 **Table S12: Comparison of the 2019 regional annual mean contrail SW, LW and net RF between the baseline simulation (with radiative heating and without contrail-**
407 **contrail overlapping) versus the simulation that accounts for the radiative effects of contrail-contrail overlapping, and another simulation that without the effects of**
408 **radiative heating interactions with the contrail plume.**

| Regional sensitivity analysis | Global | USA | Europe | East Asia | SEA | Latin America | Africa & Middle East | China | India | North Atlantic | North Pacific | Arctic Region |
|--|--------|-------|--------|-----------|-------|---------------|----------------------|-------|-------|----------------|---------------|---------------|
| 2019: Baseline simulation (Radiative heating effects ✓, contrail-contrail overlapping ✗) | | | | | | | | | | | | |
| Annual mean SW RF (mW m ⁻²) | -63.7 | -485 | -1160 | -88.9 | -83.8 | -14.7 | -20.0 | -87.8 | -35.6 | -300 | -55.0 | -10.2 |
| Annual mean LW RF (mW m ⁻²) | 126 | 900 | 2038 | 153 | 174 | 33.3 | 38.7 | 150 | 81.2 | 601 | 103 | 29.2 |
| Annual mean Net RF (mW m ⁻²) | 62.1 | 414 | 876 | 63.9 | 90.4 | 18.5 | 18.6 | 62.3 | 45.4 | 300 | 47.7 | 19.0 |
| 2019 Sensitivity analysis: Contrail-contrail overlapping (Radiative heating effects ✓, contrail-contrail overlapping ✓) | | | | | | | | | | | | |
| Annual mean SW RF (mW m ⁻²) | -57.8 | -435 | -953 | -84.4 | -81.4 | -14.7 | -21.3 | -85.2 | -34.5 | -281 | -52.9 | -9.94 |
| Annual mean LW RF (mW m ⁻²) | 117 | 810 | 1750 | 146 | 169 | 33.2 | 41.5 | 148 | 78.9 | 571 | 99.8 | 28.4 |
| Annual mean Net RF (mW m ⁻²) | 59.1 | 374 | 794 | 61.2 | 87.4 | 18.5 | 20.2 | 62.5 | 44.1 | 289 | 46.8 | 18.5 |
| Change in SW RF | -9.3% | -10% | -18% | -5.1% | -2.9% | 0.0% | 6.5% | -3.0% | -3.1% | -6.3% | -3.8% | -2.5% |
| Change in LW RF | -7.1% | -10% | -14% | -4.6% | -2.9% | -0.3% | 7.2% | -1.3% | -2.8% | -5.0% | -3.1% | -2.7% |
| Change in net RF | -4.8% | -9.7% | -9.4% | -4.2% | -3.3% | 0.0% | 8.6% | 0.3% | -2.9% | -3.7% | -1.9% | -2.6% |
| 2019 Sensitivity analysis: No radiative heating (Radiative heating effects ✗, contrail-contrail overlapping ✗) | | | | | | | | | | | | |
| Annual mean SW RF (mW m ⁻²) | -65.9 | -452 | -1214 | -81.3 | -82.0 | -14.9 | -22.1 | -87.8 | -36.1 | -318 | -56.7 | -11.8 |
| Annual mean LW RF (mW m ⁻²) | 133 | 874 | 2233 | 149 | 177 | 33.2 | 43.3 | 152 | 79.1 | 624 | 106 | 31.7 |
| Annual mean Net RF (mW m ⁻²) | 66.8 | 420 | 1016 | 67.4 | 95.0 | 18.2 | 21.2 | 64.4 | 42.8 | 305 | 49.2 | 20.0 |
| Change in SW RF | 3.5% | -6.8% | 4.7% | -8.5% | -2.1% | 1.4% | 11% | 0.0% | 1.4% | 6.0% | 3.1% | 16% |
| Change in LW RF | 5.6% | -2.9% | 9.6% | -2.6% | 1.7% | -0.3% | 12% | 1.3% | -2.6% | 3.8% | 2.9% | 8.6% |
| Change in net RF | 7.6% | 1.4% | 16% | 5.5% | 5.1% | -1.6% | 14% | 3.4% | -5.7% | 1.7% | 3.1% | 5.3% |

409



410

411 **Figure S18: Change in the percentage of flight distance forming persistent contrails (p_{contrail}) for 2019 when**
 412 **comparing the baseline scenario with the simulation without global humidity corrections applied to the**
 413 **ERA5 HRES. Basemap plotted using Cartopy 0.21.1 © Natural Earth; license: public domain.**

414

415 **S4.1 Extended humidity correction**

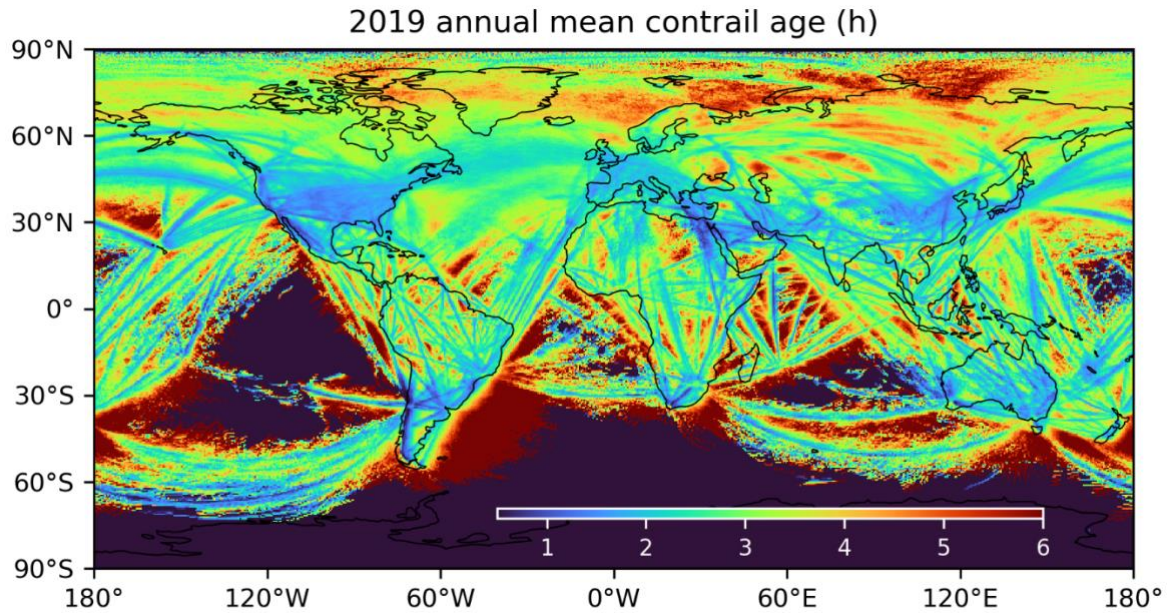
416 Fig. 8a in the main text shows significant latitude variations in the global annual mean contrail
 417 net RF when comparing between the baseline simulation with the extended global humidity
 418 corrections, c.f. Eq. (S6) to (S9) in the main text and described in Section S1.3, and the
 419 simulation without humidity corrections applied to the ERA5 HRES. Over the tropics (25°S to
 420 25°N), the extended humidity correction reduces the ISSR coverage ($a_{\text{opt}} > 1$, c.f. Eq. (S6) and
 421 Fig. S3a) but increases the RH_i inside ISSRs ($b_{\text{opt}} \approx 3$, c.f. Eq. (S6) and Fig. S3b). When taken
 422 together, the extended humidity correction increases p_{contrail} (from 2.4% without humidity
 423 correction to 2.6%, shown in Fig. S18) because a higher proportion of contrail segments survive
 424 the wake vortex phase, lifetime (+3.2%, from 2.50 to 2.58 h), and contrail net RF (+59%, from
 425 32.9 to 52.3 mW m⁻²). In the subtropics (30°N/S ± 5°), changes in p_{contrail} (from 2.5% without
 426 humidity correction to 2.3%) and contrail net RF (+2.2%, from 82.4 to 84.2 mW m⁻²) are small
 427 because effects from the smaller ISSR coverage ($a_{\text{opt}} > 1$) is balanced out by the smaller relative

428 increase in RH_i inside ISSRs ($b_{\text{opt}} \approx 1.5$). At latitudes above 35°N, the humidity correction
429 increases the ISSR coverage ($a_{\text{opt}} < 1$) and RH_i ($b_{\text{opt}} \approx 1.5$), both of which leads to significant
430 increases in p_{contrail} (from 5.7% to 7.1%) and contrail net RF (+96%, from 38.9 to 76.4 mW m⁻²).
431

432 Seasonally, the difference in monthly contrail net RF is largest during the summer (+50%
433 relative to the simulation without humidity correction) and smallest in wintertime (+40%) (Fig.
434 S17), and this is likely caused by seasonal variations in the tropopause height thereby changing
435 the proportion of flights cruising in the drier stratosphere that is not influenced by the humidity
436 correction. We also evaluate the consistency in identifying the top 5% of flights with strongly
437 warming contrails, where ~78% of flights with $\text{EF}_{\text{contrail}} > 95^{\text{th}}$ percentile in the baseline
438 simulation is also predicted to have an $\text{EF}_{\text{contrail}} > 95^{\text{th}}$ percentile in the simulation without
439 humidity correction.

440 **S4.2 Radiative heating effects**

441 Fig. 8e compare the difference in annual mean contrail cirrus net RF between the simulations
442 with and without radiative heating effects and shows a: (i) larger contrail net along established
443 flight corridors, because radiative heating increases the vertical mixing rate and τ_{contrail} ; and
444 (ii) lower contrail net RF in regions that have a higher fraction of aged contrails, i.e., east coast
445 of North and South America and away from established flight corridors (Fig. S19), because the
446 solar and terrestrial radiation heats up the contrail plume and shortens its lifetime. Radiative
447 heating also reduces the annual mean contrail net RF by 14% in Europe (Fig. 8e and Table
448 S12) because less contrails are advected into the region via the North Atlantic jet stream.



449

450 **Figure S19: The 2019 global annual mean contrail age for the simulation without radiative heating**
 451 **interactions with the contrail plume. Basemap plotted using Cartopy 0.21.1 © Natural Earth; license: public**
 452 **domain.**

453 **S4.3 Contrail-contrail overlapping**

454 Earlier studies suggested that the effects of contrail-contrail overlapping could lead to a 3%
 455 reduction in the annual mean contrail cirrus net RF globally (Sanz-Morère et al., 2021), and
 456 the contrail net RF could be reduced by up to 65% in regions with high air traffic density such
 457 as Europe (Schumann et al., 2021). CoCiP, when set up in its original form, does not account
 458 for the effects of contrail-contrail overlapping (Schumann, 2012; Schumann et al., 2012) but a
 459 recent regional study has attempted to approximate these effects with CoCiP by changing the
 460 background RSR and OLR fields resulting from the presence of contrails (Schumann et al.,
 461 2021).

462 In this study, we approximate the change in global and regional annual mean contrail net RF
 463 in 2019 due to contrail-contrail overlapping using an updated methodology of Schumann et al.
 464 (2021) and post-processing the contrail waypoint outputs from the 2019 baseline simulation.
 465 The contrail waypoint outputs provide information on each surviving contrail waypoint at a
 466 specific point in time, including the unique flight and waypoint identifier, the mid-point

467 (longitude, latitude, and altitude), dimensions (length, width, and depth) and properties (ice
468 crystal number, size, and optical depth) of contrail plume, and the local meteorology and
469 radiation. Fundamentally, contrail-contrail overlapping changes the amount of solar and
470 terrestrial radiation that reaches the contrail, where: (i) contrails at higher altitudes reflect part
471 of the incoming SDR back to space, which reduces the amount of solar irradiance in reaching
472 the contrails formed at lower altitudes; (ii) contrails at lower altitudes absorbs part of the OLR,
473 causing contrails at higher altitudes to receive a smaller fraction of the OLR; and (iii) the SW
474 component of the contrail RF at all altitudes increase the background RSR and cirrus albedo.
475 On this basis, the radiative effects of contrail-contrail overlapping can be approximated by
476 changing the background RSR and OLR fields, and the overlying cirrus optical depth above
477 the contrail (τ_{cirrus}) so that these quantities, which are used as inputs to the parametric contrail
478 RF model (Schumann et al., 2012), account for the presence of other contrails in a grid cell.

479 As CoCiP was run with model time steps (dt) of 300 s, there are 105,120 unique time slices in
480 2019. For each time slice, we: (i) obtain the global RSR and OLR fields at that specific time
481 by interpolating the ERA5 HRES radiation fields; (ii) group contrail waypoints into altitude
482 intervals of 500 m (~1640 feet); and (iii) process the contrail layers starting from the bottom to
483 the top. All contrail segments found within each altitude interval, k (~500 m), are treated as
484 one contrail layer where they do not overlap, and contrails above the layer under consideration
485 (between $k + 1$ and the highest contrail layer K) are aggregated to update the τ_{cirrus} ,

$$(\tau_{\text{cirrus}})_{i,j} = (\tau_{\text{cirrus,ERA5 HRES}})_{i,j} + \frac{\sum_{k+1}^K (\tau_{\text{contrail} \times L \times W})_{i,j}}{A_{i,j}}, \quad (\text{S10})$$

486 where i and j represents the longitude and latitude of each grid cell, τ_{contrail} is the contrail segment
487 optical depth, L and W are the contrail segment length and width, and A is the surface area of
488 each grid cell. Collectively, each contrail layer also changes the background RSR and OLR fields,

$$\Delta\text{RSR}_{i,j} = \frac{\Sigma(-\text{RF}'_{\text{SW,overlap} \times L \times W})_{i,j}}{A_{i,j}}, \text{ and} \quad (\text{S11})$$

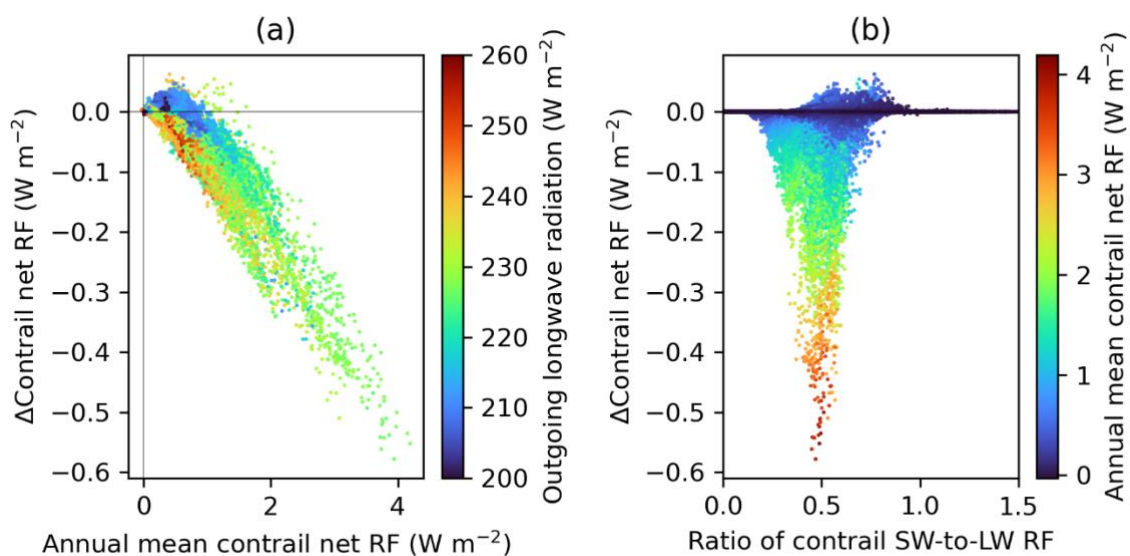
$$\Delta\text{OLR}_{i,j} = \frac{\Sigma(\text{RF}'_{\text{LW,overlap} \times L \times W})_{i,j}}{A_{i,j}}, \quad (\text{S12})$$

489 where the SW and LW RF' are computed with the updated RSR, OLR and τ_{cirrus} which
 490 accounts for the presence of other contrail cirrus, and the numerators are the sum of the contrail
 491 SW and LW radiative flux at each grid cell. Eq. (S10) to Eq. (S12) imply that: (i) the RSR and
 492 OLR received by contrails in the lowest layer ($k = 1$) is unchanged from the baseline simulation
 493 without contrail-contrail overlapping, but are expected to have a τ_{cirrus} that is larger than the
 494 baseline due to the presence of contrails above them; while (ii) contrails in the highest layer (k
 495 $= K$) are expected to have the same τ_{cirrus} as the baseline simulation, and a larger RSR (and
 496 albedo) and smaller OLR relative to the baseline simulation because of the presence of contrail
 497 cirrus below it. The updated RSR, OLR and τ_{cirrus} at each contrail waypoint are estimated
 498 using a bilinear interpolation across space (longitude and latitude). These are then used as
 499 inputs to the parametric contrail RF model (Schumann et al., 2012) to re-calculate the contrail
 500 SW and LW RF', which are subsequently used to estimate the $\text{EF}_{\text{contrail}}$ (Eq. (6) in the main
 501 text) and the global and regional annual mean contrail net RF (Eq. (7) in the main text) that
 502 accounts for contrail-contrail overlapping.

503 Using this approach, we estimate that the effects of contrail-contrail overlapping leads to a 5%
 504 reduction in the global annual mean contrail cirrus net RF (from 62.1 mW m^{-2} in the baseline
 505 simulation to 59.1 mW m^{-2}). Our estimated change in the 2019 global annual mean contrail net
 506 RF (-5%) is consistent with a parametric study that estimated a 3% reduction in the global
 507 contrail net RF due to contrail-contrail overlapping (Sanz-Morère et al., 2021). However, there
 508 are significant regional variations, where the reduction in annual mean contrail net RF is largest
 509 in regions with high air traffic activity, i.e., over the US (-9.7%) and Europe (-9.4%) (Fig. 8f

510 in the main text and Table S12). The main factors contributing to the change in annual mean
 511 contrail net RF is evaluated in Fig. S20, suggesting that contrail-contrail overlapping tends to:
 512 (i) reduce the contrail climate forcing in grid cells with a large annual mean contrail net RF ($>$
 513 1 W m^{-2}) and low ratio of annual mean contrail SW-to-LW RF (< 0.6); and (ii) increases the
 514 contrail climate forcing in grid cells with a low annual mean OLR ($< 220 \text{ W m}^{-2}$) and high ratio
 515 of annual mean contrail SW-to-LW RF (> 0.6).

516 We note that this approach to approximate the radiative effects of contrail-contrail overlapping
 517 contains limitations and simplifying assumptions, where: (i) the change in background τ_{cirrus} ,
 518 RSR, and OLR that is caused by each contrail, c.f. Eq. (S10) to (S12), is attributed to mid-point
 519 of the 3D contrail plume; (ii) it assumes maximum contrail-contrail overlapping across a
 520 vertical column in the 3D grid; and (iii) it does not account for the solar zenith angle, which
 521 can change the degree of overlapping, which in turn, changes the amount of solar radiation
 522 passing through each contrail layer. Thus, a more detailed evaluation of contrail-contrail
 523 overlapping that addresses these limitations is identified an avenue for future research.



524
 525 **Figure S20: The change in contrail climate forcing at each grid cell (y-axis) due to contrail-contrail**
 526 **overlapping versus the: (a) annual mean contrail net RF (x-axis) and the annual mean outgoing longwave**
 527 **radiation (colour bar); and (b) ratio of annual mean contrail SW-to-LW RF (x-axis) and the annual mean**
 528 **contrail net RF (colour bar).**

529 **S5 Comparison with other studies**

530 Previous studies have used the 2002 AERO2K (Eyers et al., 2005) and 2006 Aviation
 531 Environmental Design Tool (AEDT) global aviation emissions inventories (Wilkerson et al.,
 532 2010) to simulate the global contrail climate forcing (Burkhardt and Kärcher, 2011; Chen and
 533 Gettelman, 2013; Schumann et al., 2015; Bock and Burkhardt, 2016; Bier and Burkhardt,
 534 2022). A recent study from Lee et al. (2021) subsequently compiled the results from four
 535 studies (Burkhardt and Kärcher, 2011; Chen and Gettelman, 2013; Schumann et al., 2015; Bock
 536 and Burkhardt, 2016) and extrapolated the 2006 global contrail net RF to 2018 levels based on
 537 the growth in global annual flight distance flown. Table S13 summarises the methodological
 538 details and results from the different studies that quantified the global annual mean contrail
 539 cirrus net RF.

540 **Table S13: Summary of existing studies that quantified the global annual contrail cirrus net RF.**

| Study | Model | Air traffic data | Global annual mean contrail net RF (mW m ⁻²) | Remarks |
|----------------------------|-------------|------------------|--|---|
| Burkhardt & Kärcher (2011) | ECHAM4 | 2002 | 37.5 | <ul style="list-style-type: none"> Contrails initialised with dimensions of 100m (width) × 175 m (depth), and ice water content of 0.4 mg m⁻³. |
| Chen & Gettelman (2013) | CAM5 | 2006 | 57 | <ul style="list-style-type: none"> Contrails initialised with a 300 × 300m cross-sectional area, 7 μm ice particle diameter and spherical ice particle habits. Results revised in Lee et al. (2021) |
| Schumann et al. (2015) | CoCiP-CAM3 | 2006 | 63 | <ul style="list-style-type: none"> RHi_{corrected} = RHi / 0.90 Accounts for humidity exchange between contrails and the background air. |
| Bock & Burkhardt (2016) | ECHAM5 | 2006 | 56 | <ul style="list-style-type: none"> Incorporated improved parameterisation of the contrail microphysical and optical properties from Lohmann et al. (2008), Contrails initialised with constant ice crystal concentration of 150 cm⁻³. |
| Lee et al. (2021) | Multi-model | 2018 | 111 [33, 189] | <ul style="list-style-type: none"> Compiled the 2006 global annual mean contrail net RF from the above four studies and extrapolated to 2018 levels based on the growth in global air traffic. RF range captures the uncertainty in: (i) contrail cirrus radiative response; and (ii) upper tropospheric water budget and the contrail cirrus scheme. |
| Bier & Burkhardt (2022) | ECHAM5 | 2006 | 44 [31, 49] | <ul style="list-style-type: none"> Accounts for difference in nvPM activation rate and ice crystal losses in the wake vortex phase, RF range captures the differences in initial soot assumptions of 1.5 [0.5, 3.0] × 10¹⁵ kg⁻¹. |

541 In the main text, we compared our 2019 global annual mean contrail net RF (62.1 mW m^{-2})
542 with the most recent studies from: (i) Lee et al. (2021), which estimated a 2018 global contrail
543 net RF of $111 [33, 189] \text{ mW m}^{-2}$ at a 95% confidence interval; and (ii) Bier & Burkhardt (2022),
544 where the 2006 global contrail net RF from their previous study was revised down from 56
545 mW m^{-2} (Bock and Burkhardt, 2016) to 43.7 mW m^{-2} after accounting for differences in the
546 nvPM activation rate and ice crystal losses in the wake vortex phase. The comparison with Bier
547 & Burkhardt (2022) suggest that the average annual growth rate of the global contrail cirrus
548 net RF, from 43.7 mW m^{-2} in 2006 (Bier and Burkhardt, 2022) to 62.1 mW m^{-2} (this study)
549 amounting to +2.7% per annum between 2006 and 2019, was smaller than the growth in global
550 annual flight distance flown during the same period (+3.6% per annum). The 3.6% average
551 annual growth in flight distance flown was calculated based on the comparison of the 2006
552 values from the AEDT aviation emissions inventory ($38.68 \times 10^9 \text{ km}$) (Wilkerson et al., 2010)
553 with the 2019 values ($60.94 \times 10^9 \text{ km}$) provided by the Global Aviation emissions Inventory
554 based on ADS-B (GAIA) (Teoh et al., 2023).

555 The AEDT aviation emissions inventory also reported the 2006 annual fuel consumption to be
556 $188.2 \times 10^9 \text{ kg}$ (Wilkerson et al., 2010), which we then use to derive the fuel consumption per
557 flight distance flown (4.87 kg km^{-1}) and compare it with our estimates (4.60 kg km^{-1}). The
558 nvPM EI_n was not reported in the AEDT, and we approximated the fleet-aggregated nvPM EI_n
559 for 2006 ($\sim 1.15 \times 10^{15} \text{ kg}^{-1}$) with GAIA by removing flights that are flown using new
560 commercial aircraft types introduced after 2006 (i.e., Airbus A320neo, A350, A380 and the
561 Boeing 737-MAX, 747-800 and 787 families). The absolute reduction in mean fuel
562 consumption per flight distance flown (-6%) and nvPM EI_n (-11%) are expected to lower the
563 number of nvPM emitted per flight distance flown, c.f. Eq. (5) in the main text, which
564 subsequently reduces the $\text{EF}_{\text{contrail}}$ per flight distance flown (Teoh et al., 2022).

565 **References**

- 566 Agarwal, A., Meijer, V. R., Eastham, S. D., Speth, R. L., and Barrett, S. R. H.: Reanalysis-driven
567 simulations may overestimate persistent contrail formation by 100-250%, *Environ. Res. Lett.*, 17, 1–
568 14, <https://doi.org/10.1088/1748-9326/AC38D9>, 2022.
- 569 Bier, A. and Burkhardt, U.: Impact of Parametrizing Microphysical Processes in the Jet and Vortex
570 Phase on Contrail Cirrus Properties and Radiative Forcing, *J. Geophys. Res. Atmos.*, 127,
571 e2022JD036677, <https://doi.org/10.1029/2022JD036677>, 2022.
- 572 Bock, L. and Burkhardt, U.: Reassessing properties and radiative forcing of contrail cirrus using a
573 climate model, *J. Geophys. Res. Atmos.*, 121, 9717–9736, <https://doi.org/10.1002/2016JD025112>,
574 2016.
- 575 Boulanger, D., Bundke, U., Gallagher, M., Gerbig, C., Hermann, M., Nédélec, P., Rohs, S., Sauvage,
576 B., Ziereis, H., Thouret, V., and Petzold, A.: IAGOS Time series [Data set],
577 <https://doi.org/https://doi.org/10.25326/06>, 2022.
- 578 Burkhardt, U. and Kärcher, B.: Global radiative forcing from contrail cirrus, *Nat. Clim. Chang.*, 1, 54–
579 58, <https://doi.org/10.1038/nclimate1068>, 2011.
- 580 Chen, C. C. and Gettelman, A.: Simulated radiative forcing from contrails and contrail cirrus, *Atmos.*
581 *Chem. Phys.*, 13, 12525–12536, <https://doi.org/10.5194/acp-13-12525-2013>, 2013.
- 582 ECMWF: The Copernicus Programme: Climate Data Store, 2021.
- 583 Eyers, C. J., Addleton, D., Atkinson, K., Broomhead, M. J., Christou, R., Elliff, T., Falk, R., Gee, I.,
584 Lee, D. S., Marizy, C., Michot, S., Middel, J., Newton, P., Norman, P., Plohr, M., Raper, D., and
585 Stanciou, N.: AERO2K global aviation emissions inventories for 2002 and 2025, QinetiQ Eur. Comm.
586 under Contract No. G4RD-CT-2000-00382, Farnborough, Hampshire, GU14 0LX, pp., 2005., 2005.
- 587

588 Gierens, K., Matthes, S., and Rohs, S.: How Well Can Persistent Contrails Be Predicted?, 7, 169,
589 <https://doi.org/10.3390/AEROSPACE7120169>, 2020.

590 Hersbach, H., Bell, B., Berrisford, P., Hirahara, S., Horányi, A., Muñoz-Sabater, J., Nicolas, J., Peubey,
591 C., Radu, R., Schepers, D., Simmons, A., Soci, C., Abdalla, S., Abellan, X., Balsamo, G., Bechtold, P.,
592 Biavati, G., Bidlot, J., Bonavita, M., De Chiara, G., Dahlgren, P., Dee, D., Diamantakis, M., Dragani,
593 R., Flemming, J., Forbes, R., Fuentes, M., Geer, A., Haimberger, L., Healy, S., Hogan, R. J., Hólm, E.,
594 Janisková, M., Keeley, S., Laloyaux, P., Lopez, P., Lupu, C., Radnoti, G., de Rosnay, P., Rozum, I.,
595 Vamborg, F., Villaume, S., and Thépaut, J. N.: The ERA5 global reanalysis, *Q. J. R. Meteorol. Soc.*,
596 146, 1999–2049, <https://doi.org/10.1002/qj.3803>, 2020.

597 Country bounding boxes: <https://gist.github.com/graydon/11198540>, last access: 22 December 2022.

598 ICAO: The World of Air Transport in 2020, 2021.

599 Kärcher, B. and Lohmann, U.: A parameterization of cirrus cloud formation: Homogeneous freezing of
600 supercooled aerosols, *J. Geophys. Res. Atmos.*, 107, AAC 4-1, <https://doi.org/10.1029/2001JD000470>,
601 2002.

602 Koop, T., Luo, B., Tsias, A., and Peter, T.: Water activity as the determinant for homogeneous ice
603 nucleation in aqueous solutions, *Nature*, 406, 611–614, <https://doi.org/10.1038/35020537>, 2000.

604 Lee, D. S., Fahey, D. W., Skowron, A., Allen, M. R., Burkhardt, U., Chen, Q., Doherty, S. J., Freeman,
605 S., Forster, P. M., Fuglestedt, J., Gettelman, A., De León, R. R., Lim, L. L., Lund, M. T., Millar, R. J.,
606 Owen, B., Penner, J. E., Pitari, G., Prather, M. J., Sausen, R., and Wilcox, L. J.: The contribution of
607 global aviation to anthropogenic climate forcing for 2000 to 2018, *Atmos. Environ.*, 244, 117834,
608 <https://doi.org/10.1016/J.ATMOSENV.2020.117834>, 2021.

609 Lohmann, U., Spichtinger, P., Jess, S., Peter, T., and Smit, H.: Cirrus cloud formation and ice
610 supersaturated regions in a global climate model, *Environ. Res. Lett.*, 3, 045022,
611 <https://doi.org/10.1088/1748-9326/3/4/045022>, 2008.

612 Parr, W. C. and Schucany, W. R.: Minimum distance and robust estimation, *J. Am. Stat. Assoc.*, 75,
613 616–624, <https://doi.org/10.1080/01621459.1980.10477522>, 1980.

614 Petzold, A., Neis, P., Rütimann, M., Rohs, S., Berkes, F., G. J. Smit, H., Krämer, M., Spelten, N.,
615 Spichtinger, P., Nédélec, P., and Wahner, A.: Ice-supersaturated air masses in the northern mid-latitudes
616 from regular in situ observations by passenger aircraft: Vertical distribution, seasonality and
617 tropospheric fingerprint, *Atmos. Chem. Phys.*, 20, 8157–8179, [https://doi.org/10.5194/ACP-20-8157-](https://doi.org/10.5194/ACP-20-8157-2020)
618 2020, 2020.

619 Pruppacher, H. R., Klett, J. D., and Wang, P. K.: *Microphysics of Clouds and Precipitation*, 28, 381–
620 382, <https://doi.org/10.1080/02786829808965531>, 2007.

621 Reutter, P., Neis, P., Rohs, S., and Sauvage, B.: Ice supersaturated regions: Properties and validation of
622 ERA-Interim reanalysis with IAGOS in situ water vapour measurements, *Atmos. Chem. Phys.*, 20, 787–
623 804, <https://doi.org/10.5194/ACP-20-787-2020>, 2020.

624 Santer, B. D., Sausen, R., Wigley, T. M. L., Boyle, J. S., AchutaRao, K., Doutriaux, C., Hansen, J. E.,
625 Meehl, G. A., Roeckner, E., Ruedy, R., Schmidt, G., and Taylor, K. E.: Behavior of tropopause height
626 and atmospheric temperature in models, reanalyses, and observations: Decadal changes, *J. Geophys.*
627 *Res. Atmos.*, 108, ACL 1-1, <https://doi.org/10.1029/2002JD002258>, 2003.

628 Sanz-Morère, I., Eastham, S. D., Allroggen, F., Speth, R. L., and Barrett, S. R. H.: Impacts of multi-
629 layer overlap on contrail radiative forcing, *Atmos. Chem. Phys.*, 21, 1649–1681,
630 <https://doi.org/10.5194/ACP-21-1649-2021>, 2021.

631 Schumann, U.: A contrail cirrus prediction model, *Geosci. Model Dev.*, 5, 543–580,
632 <https://doi.org/10.5194/gmd-5-543-2012>, 2012.

633 Schumann, U., Mayer, B., Graf, K., and Mannstein, H.: A parametric radiative forcing model for
634 contrail cirrus, *J. Appl. Meteorol. Climatol.*, 51, 1391–1406, [https://doi.org/10.1175/JAMC-D-11-](https://doi.org/10.1175/JAMC-D-11-0242.1)
635 0242.1, 2012.

636 Schumann, U., Penner, J. E., Chen, Y., Zhou, C., and Graf, K.: Dehydration effects from contrails in a
637 coupled contrail–climate model, *Atmos. Chem. Phys.*, 15, 11179–11199, [https://doi.org/10.5194/acp-](https://doi.org/10.5194/acp-15-11179-2015)
638 15-11179-2015, 2015.

639 Schumann, U., Poll, I., Teoh, R., Koelle, R., Spinielli, E., Molloy, J., Koudis, G. S., Baumann, R.,
640 Bugliaro, L., Stettler, M., and Voigt, C.: Air traffic and contrail changes over Europe during COVID-
641 19: A model study, *Atmos. Chem. Phys.*, 21, 7429–7450, <https://doi.org/10.5194/ACP-21-7429-2021>,
642 2021.

643 Sobieralski, J. B. and Mumbower, S.: Jet-setting during COVID-19: Environmental implications of the
644 pandemic induced private aviation boom, *Transp. Res. Interdiscip. Perspect.*, 13, 100575,
645 <https://doi.org/10.1016/J.TRIP.2022.100575>, 2022.

646 Sonntag, D.: Advancements in the field of hygrometry, *Meteorol. Zeitschrift*, 3, 51–66,
647 <https://doi.org/10.1127/metz/3/1994/51>, 1994.

648 Teoh, R., Schumann, U., Majumdar, A., and Stettler, M. E. J.: Mitigating the Climate Forcing of Aircraft
649 Contrails by Small-Scale Diversions and Technology Adoption, *Environ. Sci. Technol.*, 54, 2941–2950,
650 <https://doi.org/10.1021/acs.est.9b05608>, 2020.

651 Teoh, R., Schumann, U., Gryspeerdt, E., Shapiro, M., Molloy, J., Koudis, G., Voigt, C., and Stettler,
652 M.: Aviation Contrail Climate Effects in the North Atlantic from 2016-2021., 22, 10919–10935,
653 <https://doi.org/https://doi.org/10.5194/acp-2022-169>, 2022.

654 Teoh, R., Engberg, Z., Shapiro, M., Dray, L., and Stettler, M. E. J.: A high-resolution Global Aviation
655 emissions Inventory based on ADS-B (GAIA) for 2019 - 2021 [preprint],
656 <https://doi.org/doi.org/10.5194/egusphere-2023-724>, 2023.

657 Tompkins, A. M., Gierens, K., and Rädcl, G.: Ice supersaturation in the ECMWF integrated forecast
658 system, *Q. J. R. Meteorol. Soc.*, 133, 53–63, <https://doi.org/10.1002/qj.14>, 2007.

659 Wilkerson, J. T., Jacobson, M. Z., Malwitz, A., Balasubramanian, S., Wayson, R., Fleming, G., Naiman,

660 A. D., and Lele, S. K.: Analysis of emission data from global commercial aviation: 2004 and 2006,
661 Atmos. Chem. Phys., 10, 6391–6408, <https://doi.org/10.5194/acp-10-6391-2010>, 2010.

662